

# AoI-Energy-Spectrum Optimization in Post-Disaster Powered Communication Intelligent Network via Hierarchical Heterogeneous Graph Neural Network

Hanjian Liu, Jinsong Gui

**Abstract**—This paper designs a post-disaster powered communication intelligent network (PDPCIN) to address communication disruptions caused by ground base station (GBS) failures within the post-disaster area. PDPCIN employs unmanned aerial vehicles (UAVs) to provide wireless data collection (WDC) and wireless energy transmission (WET) for affected areas and leverages low earth orbit satellites (LEO SATs) to relay UAV data to the nearest survival GBS. To ensure basic post-disaster communication while co-optimizing age of information (AoI), energy efficiency, and spectrum efficiency, intelligent synchronization-UAV (IS-UAV) architecture, AoI-based four thresholds updating (AFTU) mechanism, and Dynamic multi-LEO access (DMLA) strategy are proposed. However, three key challenges remain: time-varying task-resource imbalances, complex topology caused by multi-device scheduling, and nonlinear coupling in multidimensional metric optimization, making system optimization NP-hard. Therefore, this paper proposes a hierarchical heterogeneous graph neural networks (HHGNN) framework. It models heterogeneous device nodes and their communication relations as a hierarchical heterogeneous graph structure, integrating our defined graph sensing, exchange, and mask layer to handle the network's input, feature propagation, and output. HHGNN adopts a two-layer decision-making mechanism: the first layer optimizes UAVs' 3D trajectories and wireless energy transmission (WET) decisions, while the second layer optimizes UAV-LEO scheduling, UAV transmit power control, and subchannel allocation, based on the previous layer decisions and feedback. To search appropriate number of single-LEO SATs, we propose single-LEO SAT density optimization (S-LSDO) algorithm. Finally, we compare the proposed scheme with state-of-the-art benchmarks to validate its superior collaborative optimization of AoI, energy efficiency, and spectrum efficiency. Based on this, we derive the expressions for the expected values of AoI and stagnant AoI proportion.

**Index Terms**—Trajectory and scheduling optimization, age of Information (AoI), hierarchical heterogeneous graph neural networks (HHGNN), wireless powered communication network (WPCN), resource allocation.

## I. INTRODUCTION

For a long time, numerous regions have experienced various natural disasters, resulting in significant economic losses and even threats to human lives. Providing effective communication services to these areas is crucial for rescue operations, intelligence gathering, and post-disaster reconstruction [1]. In post-disaster areas, such as those affected by earthquakes or floods, ground-based communication infrastructure, including ground base stations (GBSs), is often partially or completely destroyed. Due to the regional coverage characteristics of cellular networks, ground terminals (GTs) located in different areas cannot directly communicate with nearby surviving GBSs, making it difficult to maintain communication links in terrestrial networks after a disaster [2].

At this point, the space-air-ground integrated network (SAGIN) provides a promising solution to this challenge. According to the International Telecommunication Union's (ITU) "Framework and overall objectives of the future development of IMT for 2030 and beyond," constructing a fully covered and intelligently coordinated SAGIN has become one of the core objectives of 6G standard evolution [3]. Meanwhile, the integration of unmanned aerial vehicles (UAVs) and low earth orbit satellites (LEO SATs) into network architectures has accelerated the maturity of SAGIN.

In ground-to-air (G2A) scenario, based on the high mobility and deployability, UAVs are typically deployed as flying base stations or aerial relays as a complementary or backup measure to provide communication coverage for ground terminals (GTs) [4]. As a result, UAVs can offer flexible communication services and deliver essential communication energy to resource-constrained post-disaster areas. However, this also brings challenges: the additional spatial degrees of freedom offered by UAVs bring potential performance improvements but also increase the complexity of network optimization; time-varying network topologies and channel conditions caused by UAV movement require frequent updates of control signals; due to the lack of prior knowledge about GT locations in post-disaster areas, UAVs must roam and search for GTs; and due to limited sensing capabilities, UAV base stations can only detect nearby GT service demands, making multi-UAV collaboration critical [5], [6], [7].

In air-to-space (A2S) scenario, compared to geostationary/medium earth orbit SATs, LEO SATs offer advantages such as low propagation loss and transmission delay, and their wide-area coverage enables them to relay data

collected by UAVs to nearby ground base stations for processing [8]. However, deploying LEO SATs into post-disaster communication networks presents several challenges: scheduling among multiple UAVs and SATs, bandwidth allocation among multiple SATs, and outage probability control [9], [10].

To summarize, three core challenges persist in post-disaster communication network optimization: 1) Supply-demand imbalance between time-varying transmission tasks and limited resources: GTs' demand for data transmission and energy supply varies over time, necessitating efficient utilization of limited resources to meet dynamic service requirements. 2) Spatiotemporal conflicts between dynamic service scheduling and resource allocation: The service scheduling topology within the SAGIN architecture are complex, requiring rational and efficient dynamic adjustments to resource allocation. 3) Nonlinear coupling among optimizations of multidimensional performance metrics: Performance indicators such as age of information (AoI), energy efficiency, and spectrum efficiency are interdependent but not linearly related, requiring a balance among these metrics to achieve global optimization.

In this paper, we integrate UAVs and LEO SATs into a post-disaster network, constructing the post-disaster powered communication intelligent network (PDPCIN). Due to the complex service and scheduling relations among GTs, UAVs, and LEO SATs, conventional deep reinforcement learning (DRL) methods struggle to solve the problem effectively. By contrast, graph neural networks (GNNs) excel at leveraging the underlying structure of irregular data or relations between different entities [11]. Moreover, since the G2A and A2S scenarios are tightly coupled, using traditional GNN techniques to achieve optimal network design is highly challenging. To address this, we propose a new hierarchical heterogeneous graph neural network (HHGNN) framework to sequentially address the communication service issues in both G2A and A2S scenarios.

Our main contributions are summarized as follows:

1) *Pragmatic System Network PDPCIN for Multi-Objective Optimization*: Section III models the post-disaster communication network and forms the SAGIN-based PDPCIN framework. Aiming at joint optimization of AoI, energy efficiency, and spectrum efficiency, this section proposes three key components: 1) AoI-Based Four Thresholds Updating (AFTU) mechanism enables each GT to dynamically switch between data-transmitting mode and energy-harvesting mode in each time slot, taking into account AoI, communication system's non-stationarity, and type switching cost. 2) Intelligent synchronization-UAV (IS-UAV) architecture supports concurrent wireless energy transmission (WET) and wireless data communication (WDC) by autonomous WET decision-making, its collection-charge synchronization mode fully exploits the parallel capabilities of UAVs, enabling fine-grained resource allocation. To our best knowledge, this is the first attempt to study the WDC and WET simultaneous control and optimization in SAGIN architectures integrating WPCN. 3) Dynamic multi-LEO access (DMLA) strategy coordinates joint scheduling across multi-UAV and multi-LEO systems while accounting for G2M communication outage probability,

thereby enhancing the robustness of post-disaster communication networks.

2) *Complex Communication Network Solution via HHGNN Framework*: Section IV formulates the global problem to achieve AoI-energy-spectrum collaborative optimization by jointly optimizing UAV's 3D continuous trajectories, WET decisions, UAV-LEO scheduling, UAV transmit power control, and SAT's subchannel allocation, under various constraints. However, solving this mixed-integer nonlinear programming (MINLP) problem independently is highly challenging due to its non-convex nature and combinatorial complexity. To address this issue, we propose the HHGNN architecture, which effectively decouples the global problem  $\mathbb{G}P$  into two layered subproblems L1 and L2 corresponding to G2A and A2S scenarios. We further analyze the equivalence of problems decoupling and formulate MDPs on L1 and L2.

3) *G3M and S-LSDO algorithm*: Section V define graph sensing layer (GSL) to aggregate concatenated features with fluctuating dimensions, graph exchange layer (GEL) to alleviate high-overhead feature transmission, and graph mask layer (GML) to smooth and mask unavailable actions, respectively, which collectively constitute G3M. Additionally, single-LEO SAT density optimization (S-LSDO) algorithm is proposed to explore the deeper relation between SAT density of single-LEO and AoI/spectrum efficiency performance. The algorithms' time complexity is calculated to verify their feasibility.

4) *Extensive Simulation Results and Analytical Derivations*: In Section VI, simulation results validate the superior performance of the proposed schemes, both in G2A and integrated G2A-space scenarios, compared to state-of-the-art benchmarks in terms of AoI, energy efficiency, and spectrum efficiency. Moreover, iterative experiments are conducted to investigate the impact of varying stagnation-age of information (S-AoI) proportions and the number of subchannels on the required SAT density of single-LEO, where S-AoI proportion denotes the fraction of total AoI attributed to UAV waiting for satellite services. Based on these experimental findings, we further derive the analytical expressions for expected values of G2A-AoI, A2S-AoI, and S-AoI proportion, respectively.

The remainder of this paper is structured as follows: Section II reviews the related works. Then, we describe the system model in Section III, followed by HHGNN's problem and MDP formulation in Section IV. The design of neural networks and algorithms in HHGNN are elaborated in Section V, and the simulation results are analyzed while the expected values are derived in Section VI. Finally, we conclude our article in Section VII.

## II. RELATED WORK

Benefiting from UAVs' high flexibility and deployability, UAV-aided wireless powered communication networks (WPCNs) integrating UAV-aided wireless data collection (WDC) and wireless energy transmission (WET) have gained prominence. [12] partitioned UAVs into dedicated data collector and energy transmitter teams, proposing a joint trajectory optimization method. To simultaneously enhance covered device count, time efficiency, and energy utilization while minimizing flying distance, [13] formulated a joint UAV



### III. SYSTEM MODEL

In this section, we first introduce the PDPCIN Architecture, and then model its G2A and A2S scenarios, respectively.

#### A. PDPCIN Architecture

As illustrated in Fig. 1, PDPCIN system encompasses both G2A and A2S scenarios. In G2A scenario, multiple UAVs are dispatched to the post-disaster area to collaboratively collect data from GTs. We denote the sets of GTs and UAVs by  $\mathcal{V}^G = \{1, \dots, n, \dots, N\}$  and  $\mathcal{V}^U = \{1, \dots, m, \dots, M\}$ , respectively. Additionally, given the resource constraints in post-disaster regions, UAVs need to conduct WET in the downlink to supply GTs with necessary energy, and GTs can switch between T-GT (data transmission) and E-GT (energy harvesting) modes.

Each GT is equipped with a single antenna and a rechargeable battery, enabling energy harvesting from UAVs or data transmission per time slot. To eliminate co-channel interference between downlink WET and uplink WDC, each UAV is equipped with different antennas operating on orthogonal frequency bands [12], [18], thereby supporting simultaneous and independent energy transfer and data collection, with autonomous WET decisions. This intelligent synchronization UAV (IS-UAV) architecture, compared to the static resource partitioning of team division UAVs (TD-UAVs) [12] or the serial processing of dynamic conversion UAVs (DC-UAV) [18], has these advantages: exploiting UAVs' parallel processing capabilities to improve resource utilization; enabling fine-grained allocation to enhance system adaptability; preventing communication outages due to energy depletion, thereby improving overall robustness. The relevant comparison experiments are conducted in Section VI.

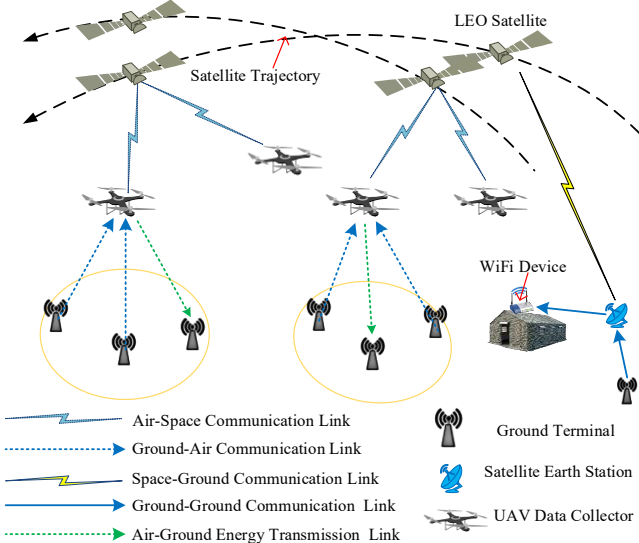


Fig. 1. Post-disaster powered communication intelligent network.

Each UAV is equipped with a replaceable battery. If the current battery is depleted, it can be replaced to resume data collection tasks. Notably, owing to the absence of prior information regarding GT locations, constrained UAV battery capacity, and UAVs' inherent limitations in sensing range and coverage, trajectory planning plays a vital role in WDC and WET. Meanwhile, UAVs are equipped with energy harvesting

boards to gather renewable energy, such as solar power. To rationally utilize the limited battery resources, ensure seamless data transmission by UAVs, and facilitate subsequent neural network decision-making based on energy status, the replaceable battery energy is exclusively used for non-communication behaviors (e.g., UAV mobility and energy transmission), whereas the harvested energy is reserved for communication operations—specifically, for transmitting data to LEO SATs.

In the A2S scenario, an ultra-dense LEO SAT constellation is considered, with multiple LEOS covering the target area. SATs in each LEO periodically passes over the area, achieving seamless coverage. Therefore, UAVs can select one LEO SAT to access in each time slot from among multiple observable LEO SATs. These LEO SATs can relay the data collected from UAVs to ground base stations (GBSs) that have not been affected by the disaster for further processing. UAVs can simultaneously receive data from GTs and transmit data to LEO SATs, adopting store-and-forward mode where data received from GTs in one time slot is forwarded to LEO SATs in the next. To improve spectrum efficiency and system capacity, UAVs employ NOMA to access LEO SATs. Assume that G2A communication uses C-band and A2S communication uses Ka-band, so the two do not interfere with each other [28].

#### B. G2A Transmission Scenario Description

##### 1) Sensing and Coverage Model

We assume the position of GT- $n$  is denoted by  $\mathbf{q}_n^G(t) = (x_n^G(t), y_n^G(t), z_n^G(t)) \in \mathbb{R}^3$ . In slot  $t$ , the position of UAV- $m$  is denoted by  $\mathbf{q}_m^U(t) = (x_m^U(t), y_m^U(t), z_m^U(t)) \in \mathbb{R}^3$ . Moreover, we assume that all GTs are remain on the level ground, i.e.,  $z_n^G = 0$ . The flight altitude of UAVs is dynamically adjusted. GTs transmit service requests and location coordinates via a control and non-payload communications (CNPC) link. Due to signal attenuation, UAVs can serve GTs only within a limited range. Similarly, each UAV can sense other UAVs within a certain range [29]. The maximum ranges for UAVs to detect GTs and other UAVs are denoted by  $O_S^G$  and  $O_S^U$ , respectively. In slot  $t$ , UAV- $m$  can detect GT- $n$  only if  $d_{n,m}(t) \leq O_S^G$ , where  $d_{n,m}(t) = \|\mathbf{q}_m^U(t) - \mathbf{q}_n^G(t)\|$  is their mutual distance. UAV- $m$  and UAV- $i$  can detect each other only if their mutual distance  $d'_{m,i}(t) = \|\mathbf{q}_m^U(t) - \mathbf{q}_i^U(t)\|$  satisfies  $d'_{m,i} \leq O_S^U$ . Moreover, UAV- $m$  can collect data from GT- $n$  or GT- $n$  can harvest energy from UAV- $m$  only if  $d_{n,m}(t) \leq O_C^U$ , where  $O_C^U$  is UAVs' coverage range satisfying  $O_C^U < O_S^G$ . Consequently, each UAV has only partial system observation. Since UAVs hover over the area during each time interval, their observations change over time. To describe the connectivity among GTs and UAVs at each slot  $t$ , we define three matrices  $\mathbf{G}(t) \in \{0,1\}^{N \times M}$ ,  $\mathbf{U}(t) \in \{0,1\}^{M \times M}$ , and  $\mathbf{C}(t) \in \{0,1\}^{N \times M}$ . In slot  $t$ ,  $(n, m)$ -th entry of  $\mathbf{G}(t)$ , denoted by  $g_{n,m}(t)$ , is 1 if GT- $n$  is detected by UAV- $m$ ; similarly,  $u_{i,m}(t) = 1$  if UAV- $i$  is detected by UAV- $m$ ;  $c_{n,m}(t) = 1$  if GT- $n$  is within UAV- $m$ 's coverage range and can be served by UAV- $m$ ; all are 0 otherwise.

##### 2) AoI-based Four Thresholds Updating

UAVs evaluate information freshness using the AoI metric for each GT. In PDPCIN system, GTs' data packet generation follows the Poisson distribution, we refine the calculation of

AoI to the packet level, and in slot  $t$  GT- $n$ 's AoI  $a_n^G(t)$  is computed as

$$a_n^G(t) = \sum_{i=1}^{I_n^G(t)} a_{n,i}^G(t), \quad (1)$$

$$a_{n,i}^G(t) = \begin{cases} 0, & \text{if received,} \\ a_{n,i}^G(t-1) + 1, & \text{otherwise,} \end{cases} \quad (2)$$

where  $a_{n,i}^G(t)$  is the AoI of GT- $n$ 's  $i$ -th packet at the end of slot  $t$ , and  $I_n^G$  is the total number of packets generated by GT- $n$  up to the end of slot  $t$ . The average AoI of all GTs in slot  $t$  is represented as  $A^G(t) = \frac{\sum_{n=1}^N a_n^G(t)}{N}$ . It is worth noting that the above GTs' AoI calculation method is also applicable to UAVs, with  $a_m^U(t)$  denotes UAV- $m$ 's AoI and  $A^U(t)$  denotes average AoI of all UAVs in slot  $t$  respectively.

To allow GTs with higher AoI to transmit data more quickly and reserve energy for those with less urgent tasks, we

$$\epsilon_n(t) = \begin{cases} 0, & \text{if } B_n^G(t) \geq B_T \text{ or } (B_E < B_n^G(t) < B_T \text{ and } a_n^G(t) \geq (1 + \xi)A^G(t)) \\ 1, & \text{if } B_n^G(t) \leq B_E \text{ or } (B_E < B_n^G(t) < B_T \text{ and } a_n^G(t) \leq (1 - \xi)A^G(t)) \\ e_n(t-1), & \text{if } B_E < B_n^G(t) < B_T \text{ and } (1 - \xi)A^G(t) < a_n^G(t) < (1 + \xi)A^G(t) \end{cases} \quad (3)$$

It is worth mentioning that unlike the widely-used single-threshold method (causing frequent type switching), e.g., [16], or the newly proposed double-threshold based WN type updating approach (reducing updates via fixed thresholds) [18], our dynamic  $\xi$  scaling in (3) ensures efficient AoI control in non-stationary environments while minimizing unnecessary type switches in stable conditions, improving flexibility and reliability.

### 3) G2A Communication Model

Let  $P_{n,m}^{LoS}(t) = (1 + a \exp(-b(\beta_{n,m}(t) - a)))^{-1}$  denote the probability of a line-of-sight (LoS) link between GT- $n$  and UAV- $m$  in slot  $t$ , where the elevation angle is given by  $\beta_{n,m}(t) = \sin^{-1}(h/d_{n,m}(t))$ , and parameters  $a$  and  $b$  are constants determined by environmental characteristics. Accordingly, the probability of a non-line-of-sight (NLoS) link is  $P_{n,m}^{NLoS}(t) = 1 - P_{n,m}^{LoS}(t)$ . The channel gain between GT- $n$  and UAV- $m$  in slot  $t$  is calculated as [30]

$$h_{n,m}(t) = P_{n,m}^{LoS}(t)H_0d_{n,m}(t)^{-\alpha_L} + P_{n,m}^{NLoS}(t)H_0d_{n,m}(t)^{-\alpha_N}, \quad (4)$$

where  $H_0$  denotes the channel gain mean value at a 1 m reference distance, with  $\alpha_L$  and  $\alpha_N$  ( $0 < \alpha_L < \alpha_N$ ) serving as path-loss exponents for LoS link and NLoS connections. Directional antennas are used to reduce interference and improve UAV energy efficiency. As all UAVs share the spectrum, overlapping coverage causes inter-UAV interference, thus degrading link quality. Thus, each GT always select the nearest UAV covering it. Define a scheduling matrix  $\mathbf{S}(t)$  with entry  $s_{n,m}(t) = 1$  if GT- $n$  is scheduled to UAV- $m$  in slot  $t$ , else 0. Each GT accesses at most one UAV per slot, satisfying:  $\sum_{m=1}^M s_{n,m}(t) \leq 1$ . A frequency division multiple access (FDMA) scheme is adopted in G2A scenario, where the total GT-UAV spectrum is divided into  $Y^U$  equal subchannels of width  $W^U$ , and each GT can be assigned to at most one subchannel. The uplink signal-to-interference-and-noise ratio (SINR) from GT- $n$  to UAV- $m$  is computed by

$$\gamma_{n,m}(t) = \frac{s_{n,m}(t)h_{n,m}(t)P^G}{\sum_{i \in \mathcal{V}^G, i \neq n} c_{i,m}(t)s_{i,j}(t)h_{i,m}(t)P^G + \mathbb{N}_0 W^U}, \quad (5)$$

where  $\mathbb{N}_0$  is the power spectral density of the additive white Gaussian noise (AWGN), and  $P^G$  is GTs' fix transmit power.

propose AFTU to update GT types. Denote  $\epsilon_n(t)$  as GT- $n$ 's type, where 0 represents a T-GT and 1 an E-GT. According to AGTU rule, GT- $n$  updates its type at the end of slot  $t$  by (3). Let  $B_n^G(t)$  denote GT- $n$ 's battery energy level at slot  $t$  end, with threshold  $B_E$  (E-GT) and  $B_T$  (T-GT) satisfying  $P^G \tau < B_E < B_T$ , where  $P^G$  and  $\tau$  are T-GT's fixed transmit power and time slot duration. Coefficient  $\xi \in [0,1]$  is the weight of GT type updating activity, with a lower value indicating increased frequent GT type updating to adapt to a non-stationary environment. From (13), GT type updating follows four thresholds: 1) power outside  $B_E$  or  $B_T$  triggers an update; 2) if not, update if AoI exceeds  $(1 \pm \xi)A^G(t)$ . Otherwise, the remains unchanged. Notably, global  $A^G(t)$  is typically replaced by local  $\hat{A}^G(t)$  calculated by GTs based on all GTs' AoI within their perceptible range, as global values are usually inaccessible.

The data volume transmitted by GT- $n$  and collected by UAV- $m$  in slot  $t$  are obtained as

$$D_n^G(t) = \sum_{m=1}^M W^U \log(1 + \gamma_{n,m}(t))\tau, \quad (6)$$

$$D_m^U(t) = \sum_{n=1}^N W^U \log(1 + \gamma_{n,m}(t))\tau. \quad (7)$$

Accordingly, the data volume collected by UAV- $m$  in slot  $t$  denotes by  $D_m^U(t) = \sum_{n=1}^N s_{n,m} D_n^G(t)$ . To address the situation where scheduled GTs outnumber available subchannels, we propose a AoI-fairness metric  $q_n(t)$  (with a higher value indicating higher priority) that jointly considers AoI and service fairness. It is calculated by  $q_n(t+1) = \frac{\kappa a_n^G(t)}{A^G(t)} - \frac{(1-\kappa)N\hat{D}_n^G(t)}{\hat{D}^G(t)}$ , where  $\hat{D}_n^G(t) = \sum_{i=1}^t D_n^G(i)$  is total data amount transmitted by GT- $n$  up to slot  $t$ ,  $\hat{D}^G(t) = \sum_{n=1}^N c_{n,m}(t)\hat{D}_n^G(t)(1 - \epsilon_n(t))$  is total transmitted data amount up to slot  $t$  of GTs which request to access UAV- $m$  in slot  $t+1$ , and  $\kappa \in [0,1]$  is the AoI-fairness balance coefficient with lower values tending to fair scheduling and higher values tending to low-AoI scheduling. Furthermore, we employ long-term Jain's fairness index to quantify the fairness of UAV services, computed as  $F(t) = \frac{(\sum_{n=1}^N \hat{D}_n^G(t))^2}{N \sum_{n=1}^N (\hat{D}_n^G(t))^2}$ , where the  $F(t) \in [\frac{1}{N}, 1]$ , with higher values indicating greater fairness.

### 4) UAVs' Energy Transmissions Model

Let  $Z_m(t) \in \{0, 1\}$  denote UAV- $m$ 's WET decision in slot  $t$ : it transmits energy with fixed power  $P_E^U > 0$  only if  $Z_m(t) = 1$ . Each E-GT uses a non-linear energy harvester that converts received Radio Frequency (RF) power  $p_e$  into stored direct current (DC) power  $\bar{P}(p_e)$  via a non-linear function as follows [31]:

$$\bar{P}(p_e) = \begin{cases} 0, & p_e \in [0, P_{\text{sen}}), \\ f(p_e), & p_e \in [P_{\text{sen}}, P_{\text{sat}}), \\ f(P_{\text{sat}}), & p_e \in [P_{\text{sat}}, +\infty), \end{cases} \quad (8)$$

where  $P_{\text{sen}}$  and  $P_{\text{sat}}$  with  $0 < P_{\text{sen}} < P_{\text{sat}}$  denote the energy harvester's sensitivity power and saturation power, and  $f(\cdot)$  is a non-linear power transform function obtained via curve fitting. From (7), no DC power is harvested if  $p < P_{\text{sen}}$  and it saturates at  $p \geq P_{\text{sat}}$ . E-GT- $n$ 's harvested energy in slot  $t$  is

$$E_n^{GH}(t) = \epsilon_n(t)\bar{P}\left(\sum_{m=1}^M P_E^U Z_m(t)h_{n,m}(t)\right)\tau. \quad (9)$$

Owing to the practically high value of  $P_{\text{sen}}$  (e.g., -10 dBm [32]), UAVs with  $Z_m(t) = 1$  must locate near E-GT- $n$  for non-zero energy harvesting. Denote  $B_{\text{max}}^G$  as the GT battery capacity and  $E_n^{Gc}(t) = \sum_{m=1}^M s_{n,m}(t) P^G \tau$  as T-GT- $n$ 's energy consumption in slot  $t$ , GT- $n$ 's remaining energy at the beginning of time slot  $t + 1$  is updated as

$$B_n^G(t+1) = \min(B_n^G(t) + E_n^{Gh}(t) - E_n^{Gc}(t), B_{\text{max}}^G). \quad (10)$$

Due to  $P^G \tau < B_E$  in AGTU to prevent GTs from transmitting data under insufficient energy,  $B_n^G(t+1)$  will not be lower than 0.

### 5) G2A Energy Consumption Model

In G2A scenario, UAV energy consumption primarily arises from movement, WET, and WDC. From [33], UAV- $m$ 's propulsion power consumption in slot  $t$  depends on its velocity  $V_m^U(t) \triangleq \frac{1}{\tau} \|q_m^U(t+1) - q_m^U(t)\|$  as follows:

$$P_{\text{pro}}(V_m^U(t)) = P_0 \left( 1 + \frac{3V_m^U(t)^2}{U_{\text{tip}}^2} \right) + \frac{1}{2} d_0 \rho s A V_m^U(t)^3 + P_j \left( \sqrt{1 + \frac{V_m^U(t)^4}{4v_0^4}} - \frac{V_m^U(t)^2}{2v_0^2} \right)^{\frac{1}{2}}, \quad (11)$$

where the details of the constant parameters  $P_0$ ,  $P_j$ ,  $U_{\text{tip}}$ ,  $v_0$ ,  $d_0$ ,  $\rho$ ,  $s$  and  $A$  are given in [33]. Hence, UAV- $m$ 's total energy consumption in slot  $t$  is:

$$E_m^{Uc}(t) = (\sum_{n=1}^N s_{n,m}(t) P_C^U + P_{\text{pro}}(V_m^U(t)) + Z_m(t) P_E^U) \tau, \quad (12)$$

where  $P_C^U$  is the fixed WDC consumption power at each UAV. Accordingly, UAV- $m$ 's battery energy level at the beginning of slot  $t + 1$  is calculated as

$$B_m^U(t+1) = \max(B_m^U(t) - E_m^{Uc}(t), 0). \quad (13)$$

It is assumed that every UAV starts with a full charge, such that  $B_m^U(0) = B_{\text{max}}^U$ , where  $B_{\text{max}}^U$  denotes UAV battery capacity.

## C. A2S Transmission Scenario Description

We consider a set  $\mathcal{K} = \{1, \dots, k, \dots, K\}$  of LEOs and sets  $\mathcal{V}^k = \{1, \dots, l^k, \dots, L^S\}$  of LEO SATs in LEO- $k$ , with  $|\mathcal{V}^k| = L^S, \forall k \in \mathcal{K}$ . Without loss of generality, assume all SATs move in uniform circular motion with period  $\mathcal{T}$ , and arc length between any adjacent LEO SATs are equal. SATs in each LEO serve the area of interest uninterruptedly in turns, with each UAV attempting to access only to the closest LEO SAT in each LEO [34]. The area of interest (e.g., 2 km radius) is much smaller than the SAT beam coverage range (e.g., 580 km radius) [35] and the arc length between adjacent LEO SATs in the same LEO (e.g., 1976 km). Thus, for all UAVs, the nearest LEO SAT per orbit is identical within a given time slot.

In DMLA system, the spectrum allocation mode, adopted to enhance spectrum efficiency and system capacity, involves three key steps: 1) Dynamic SAT-UAV Connection: each UAV is strategically scheduled to the corresponding LEO and establishes connection with the LEO's closest SAT dynamically based on their specific communication requirements, ensuring adaptive resource utilization. 2) Subchannel Partitioning: The available frequency band is divided into smaller subchannels to enable flexible allocation and sharing. These subchannels are strategically assigned in different proportions to each LEO's SAT closest to the area of interest. 3) NOMA-based Subchannel Sharing: UAVs connected to the same LEO SAT employ NOMA technology to

share the allocated subchannels at dynamic transmit power, maximizing spectrum reuse. Details of UAV-LEO scheduling, subchannel allocation, and UAV power control strategies are provided in Section IV and V.

### 1) Single-LEO Coverage Model

We employ Single-LEO coverage model to derive the per-cycle SAT service duration for UAVs, with the multi-LEO case following similarly. The angle between the UAV- $m$  and SAT- $l^k$  can be obtained as [22]

$$\omega_A = \arccos \left( \frac{d_E + h_k}{\hat{d}_{m,l^k}} \sin \omega_C \right), \quad (14)$$

where  $d_E$  is earth radius,  $h_k$  is LEO- $k$ 's height,  $\hat{d}_{m,l^k}$  is the distance between UAV- $m$  and SAT- $l^k$ , and  $\omega_C$  is the angle for SAT- $l^k$ 's coverage. Note that SATs cease service to UAVs when their elevation angle falls below the predefined minimum threshold  $\omega_A$ .  $\omega_C$  is given by

$$\omega_C = \arccos \left( \frac{d_E}{d_E + h_k} \cos \omega_A \right) - \omega_A. \quad (15)$$

Since the movement range of UAVs is negligible compared to  $d_E$  and  $h_k$ , the coverage time  $T_{m,l^k}$  of UAV- $m$  by SAT- $l^k$  is calculated as

$$T_{m,l^k} = \frac{2(d_E + h_k)\omega_C}{V^S}, \quad (16)$$

where  $V^S$  is LEO SATs' orbital velocity.

### 2) A2S Channel Model

The LoS/NLoS channel in the commonly used Ka-band between UAV- $m$  and SAT- $l^k$  in slot  $t$  can be expressed as

$$h_m^{l^k}(t) = \omega_m^{l^k}(t) \left( \sqrt{\frac{\lambda_m^{l^k} f_m^{l^k}}{\lambda_m^{l^k} + 1}} h_{m,l^k}^{\text{LOS}} + \sqrt{\frac{f_m^{l^k}}{\lambda_m^{l^k} + 1}} h_{m,l^k}^{\text{NLOS}} \right), \quad (17)$$

where  $h_{m,l^k}^{\text{LOS}}$  and  $h_{m,l^k}^{\text{NLOS}}$  are the LOS and NLOS components,  $\omega_m^{l^k}(t)$  is the SAT receiving antenna gain,  $f_m^{l^k}$  is the large-scale fading factor, and  $\lambda_m^{l^k}$  is the small-scale fading factor (i.e., the Rician factor). According to [36],  $\omega_m^{l^k}(t)$  is expressed by

$$\omega_m^{l^k}(t) = \frac{\mathcal{J}_1(\zeta_m^{l^k})}{2\zeta_m^{l^k}} + 36 \frac{\mathcal{J}_3(\zeta_m^{l^k})}{(\zeta_m^{l^k})^3}, \quad (18)$$

where  $\mathcal{J}_1$  and  $\mathcal{J}_3$  are the first kind of Bessel functions of orders one and three, respectively.  $\zeta_m^{l^k}$  is expressed by

$$\zeta_m^{l^k} = \frac{\pi d_s f_c^S}{c} \sin(\theta_m^{l^k}), \quad (19)$$

where  $d_s$  is LEO SAT's circular antenna array diameter,  $f_c^S$  is the LEO SAT network's carrier center frequency, and  $\theta_m^{l^k}$  is the off-axis of the boresight of SAT- $l^k$  to UAV- $m$ . According to [37], [38],  $f_m^{l^k}$  is expressed by

$$f_m^{l^k} = \left( \frac{c}{4\pi f_c^S d_0} \right)^2 \cdot \frac{G_m^{l^k}}{\kappa W_{UL} T_N} \cdot \frac{1}{r_m^{l^k}}, \quad (20)$$

where  $\left( \frac{c}{4\pi f_c^S d_0} \right)^2$  is the free space loss with  $d_0$  being the orbit altitude of SAT- $l^k$ ,  $\kappa$  is the Boltzman's constant, and  $T_N$  is the temperature of the received noise. In addition,  $G_m^{l^k}$ ,  $W_{UL}$ , and  $r_m^{l^k}$  are transmission antenna gain, carrier bandwidth, and rain attenuation coefficient between UAV- $m$  and SAT- $l^k$ .  $r_m^{l^k}$ 's power gain in dB follows log-normal random distribution (i.e.,  $r_{m,l^k}^{\text{dB}} = 20 \log_{10} r_m^{l^k}$  and  $\ln(r_{m,l^k}^{\text{dB}}) \sim \mathcal{N}(\mu_r, \sigma_r^2)$ ) [39].  $h_{m,l^k}^{\text{NLOS}}$  follows a complex Gaussian distribution, i.e.,

$h_{m,l^k}^{NLOS} \sim \mathcal{CN}(0, \nu_{m,l^k}^{NLOS})$ . Thus,  $h_m^{l^k}(t)$  can be simplified as

$$h_m^{l^k}(t) \sim \mathcal{CN}\left(\omega_m^{l^k}(t) \sqrt{\frac{\lambda_m^{l^k} f_m^{l^k}}{\lambda_m^{l^k} + 1}} h_{m,l^k}^{LOS}, \frac{(\omega_m^{l^k}(t))^2 f_m^{l^k}}{\lambda_m^{l^k} + 1} \nu_{m,l^k}^{NLOS}\right).$$

### 3) Multi-LEO NOMA Model

In wireless communication scenario, outage probability is defined as the probability that instantaneous rate falls below a threshold, leading to communication quality degradation or connection loss, directly affecting AoI. As a critical metric, it evaluates wireless links reliability under diverse channel conditions. In NOMA systems, outage probability holds particular significance due to the non-orthogonal sharing of time-frequency resource among users [40], exacerbating inter-user interference and increasing AoI. Therefore, effective management of outage probability is essential for ensuring reliable communication in NOMA systems. Denote  $\mathcal{J}(t) = \{J^1(t), \dots, J^k(t), \dots, J^K(t)\}$  as the number of UAVs accessing to each LEO's SATs in slot  $t$ . The outage probability at SAT- $l^k$  is given by:

$$P_{l^k}^O = 1 - \Pr\{\phi_1^{l^k} \cap \dots \cap \phi_m^{l^k} \cap \dots \cap \phi_{j^k(t)}^{l^k}\}, \quad (21)$$

where  $\phi_m^{l^k}$  represents the event that UAV- $m$ 's signal has been decoded correctly by SAT- $l^k$  and  $\Pr\{\cdot\}$  is the possibility of the event occurring. Define an outage matrix  $\mathcal{O}(t)$  of which the  $(m, k, l)$ -th entry  $o_m^{l^k}(t) = 0$  if  $R_m^{l^k}(t) \geq \hat{R}_m^{l^k}$  and 1 otherwise, where  $\hat{R}_m^{l^k}$  is the minimum data rate required for SAT- $l^k$  to decode UAV- $m$ 's signal [41]. Intuitively, coordinating the rates of all UAVs is crucial to reduce outages: excessively high rates intensify interference, disrupting other UAVs' decoding, while too low rates cause self-outages.

To mitigate successive interference cancellation (SIC) process's interference effects, assume the channel gains of UAVs accessing the same SAT be sorted in descending order as  $|h_1^{l^k}(t)|^2 \geq |h_2^{l^k}(t)|^2 \geq \dots \geq |h_m^{l^k}(t)|^2 \geq \dots \geq |h_{j^k(t)}^{l^k}(t)|^2$ . During decoding of UAV- $m$ 's message, signals from UAV- $i$  ( $i < m$ ) are canceled, while signals from UAV- $j$  ( $j > m$ ) are treated as noise. Define a scheduling matrix  $\mathcal{S}(t)$  of which the  $(m, k, l^k)$ -th entry  $s_m^{l^k}(t) = 1$  if UAV- $m$  connects to SAT- $l^k$  in slot  $t$  and 0 otherwise, satisfying  $\sum_{k=1}^K \sum_{l^k \in \mathcal{V}^k} s_m^{l^k}(t) \leq 1$ . More, assume there are  $Y^S$  subchannels between UAVs and LEO SATs, where  $\{\rho_1(t), \dots, \rho_k(t), \dots, \rho_K(t)\}$  denotes the subchannel ratios (with  $\sum_{k \in \mathcal{K}} \rho_k \leq 1$ ) of each LEO's allocated subchannels to the total subchannels in slot  $t$ . Each UAV's total transmit power is evenly distributed across allocated subchannels. Considering outage probability, the SINR of UAV- $m$  connected to SAT- $l^k$  in each subchannel is calculated as:

$$\gamma_m^{l^k} = \frac{s_m^{l^k}(t) h_m^{l^k}(t) P_m^U(t)}{\sum_{i=m+1}^{j^k(t)} h_i^{l^k}(t) P_m^U(t) + \sum_{i=1}^{m-1} o_m^{l^k}(t) h_i^{l^k}(t) P_m^U(t) + W^S N_0}, \quad (22)$$

where  $W^S$  is UAV-SAT subchannel bandwidth,  $P_m^U(t)$  is UAV- $m$ 's per-subchannel transmit power. Accordingly, UAV- $m$ 's transmission capacity and its actual throughput in slot  $t$  can be denoted as:

$$\begin{aligned} \dot{D}_m^U(t) &= Y^S W^S \sum_{k=1}^K \sum_{l^k \in \mathcal{V}^k} \rho_k(t) \log_2(1 + \gamma_m^{l^k}) \hat{\tau}_m(t), \quad (23) \\ \hat{D}_m^U(t) &= \min(D_m^U(t), \dot{D}_m^U(t)), \quad (24) \end{aligned}$$

where  $\hat{\tau}_m(t) = \min\left(\frac{\hat{B}_m^U(t) + E_m^{Uh}(t)}{P_m^U(t)}, \tau\right)$  is the actual duration of data transmission,  $\hat{B}_m^U(t)$  is energy storage of UAV- $m$ 's energy harvesting board at the beginning of slot  $t$ , and  $E_m^{Uh}(t)$  is UAV- $m$ 's harvested energy in slot  $t$ . UAV- $m$ 's total transmission energy consumption in slot  $t$  is  $\hat{E}_m^{Uc}(t) = \rho_k(t) Y^S P_m^U(t) \hat{\tau}_m(t)$ .

## IV. PROBLEM AND MDP FORMULATION

In this section, we first analyze the problem-solving difficulty and then introduce the HHGNN framework. Subsequently, we model the global problem  $\mathbb{G}\mathbb{P}$ , subproblems  $\mathbb{L}1$ , and  $\mathbb{L}2$ , analyze the feasibility of their decoupled solutions, and finally design the MDPs for  $\mathbb{L}1$  and  $\mathbb{L}2$ .

### A. HHGNN Framework

The target of this work is to jointly optimize UAVs' trajectories  $\mathbf{Q} = \{\mathbf{q}_m^U(t)\}$ , WET decisions  $\mathbf{Z} = \{Z_m(t)\}$ , UAV-LEO scheduling  $\mathcal{S} = \{s_m^{l^k}(t)\}$ , UAV transmit power  $\mathbf{P} = \{P_m^U(t)\}$ , and SAT subchannels allocation  $\boldsymbol{\rho} = \{\rho_k(t)\}$ , with the aim to improve AoI of all GTs/UAVs, energy and bandwidth utilization efficiency and so on.

Classical combinatorial optimization or DRL methods may struggle to jointly optimize the five variables due to three critical limitations: 1) The dynamic path planning and limited coverage range of multiple UAVs, along with the multi-choice scheduling from multiple UAVs to multiple LEO SATs, result in a complex network topology. Coupled with the interdependencies among optimization variables, this renders the computational complexity of solution algorithms intractable. 2) The UAV's limited sensing range prevents a centralized controller from determining all UAVs'  $\mathbf{Q}$ ,  $\mathbf{Z}$ ,  $\mathcal{S}$ , and  $\mathbf{P}$ , while SAT subchannels  $\boldsymbol{\rho}$  are contention-based resources among UAVs and cannot be jointly optimized with UAV characteristic variables in a decentralized manner. 3) As the PDPCIN framework divides the SAGIN architecture into G2A and A2S scenarios, UAV data transmission in the latter scenario unidirectionally depends on data collection in the former, such that action decisions in the former affect the environment states in the latter, making it impossible to use a single neural network for unified decision-making across all five variables.

Therefore, we propose the HHGNN framework using hierarchical decoupling: First, formulate the global optimization problem ( $\mathbb{G}\mathbb{P}$ ), then decompose it into two subproblems ( $\mathbb{L}1$  and  $\mathbb{L}2$ ) through the PDPCIN framework. Each subproblem is modeled as a MDP, with variables  $\mathbf{Q}$ ,  $\mathbf{Z}$ ,  $\mathcal{S}$ ,  $\mathbf{P}$ , and  $\boldsymbol{\rho}$  allocated to the respective MDPs. The PDPCIN topology is represented as a heterogeneous graph, where  $\mathbb{L}1$  and  $\mathbb{L}2$  are solved sequentially using multi-agent reinforcement learning (MARL) and single-agent reinforcement learning (SARL) architectures to achieve an indirect global solution. Moreover, by integrating the HHGNN framework, we further design S-LSDO algorithm to optimize SAT Density. Detailed methodology follows.

### B. Problem Formulation

To improve the overall system performance, we need to clarify the data transmission and energy consumption of each layer. In G2A scenario, the total data volume transmitted from

GTs to UAVs is  $D^G(t) = \sum_{m=1}^M D_m^U(t)$ , and the total energy consumption is  $E(t) = \sum_{n=1}^N E_n^{Gc}(t) + \sum_{m=1}^M E_m^{Uc}(t)$  in slot  $t$ . Accordingly, in G2A scenario, the total transmission capacity and data volume transmitted from UAVs to LEO SATs are  $D^U(t) = \sum_{m=1}^M \dot{D}_m^U(t)$  and  $\hat{D}^U(t) = \sum_{m=1}^M \hat{D}_m^U(t)$ , and the total energy consumption is  $\hat{E}(t) = \sum_{m=1}^M \hat{E}_m^{Uc}(t)$  in slot  $t$ . Thus, the global optimization problem can be formulated as follows:

$$\mathbb{G}\mathbb{P}: \max_{\mathbf{Q}, \mathbf{Z}, \mathcal{S}, \mathbf{P}, \boldsymbol{\rho}} \frac{\hat{D}^U(t)}{\beta(E(t) + \hat{E}(t))(A^G(t) + A^U(t))}, \quad (25)$$

s. t. (3), (9), (12), C1-C12,

where  $\beta$  is a positive scaling factor used to balance the magnitudes of denominator and numerator, constraint C1 to C12 will be introduced later in L1 and L2.

Problem  $\mathbb{G}\mathbb{P}$  involves multiple optimization variables and segmented data transmission, classifying it as a MINLP problem. Treating it as a monolithic optimization problem becomes computationally intractable. According to HHGNN Framework, we further decouple problem  $\mathbb{G}\mathbb{P}$  into two layered subproblems L1 and L2. The global solution is indirectly obtained through iterative subproblem resolutions. The formulation of the first layer optimization subproblem L1 is:

$$\mathbb{L}1: \max_{\mathbf{Q}, \mathbf{Z}} \frac{D^G(t)}{\beta E(t) A^G(t)}, \quad (26)$$

$$\text{s. t. (3), (9), (12)}$$

$$\|\mathbf{v}_m(t)\|_2 \leq v_{max}^U, \forall m \in \mathcal{V}^U, \quad (C1)$$

$$q_m^U(t) \in [0, L_E]^2, \forall m \in \mathcal{V}^U, \quad (C2)$$

$$\sum_{m=1}^M s_{n,m}(t) \leq 1, \forall n \in \mathcal{V}^G, \quad (C3)$$

$$\sum_{n=1}^N s_{n,m}(t) \leq Y^U, \forall m \in \mathcal{V}^U, \quad (C4)$$

$$B_m^U(t_{end}) \geq B_{min}^U, \forall m \in \mathcal{V}^U, \quad (C5)$$

$$d'_{m,i}(t) \geq d_{min}, \forall m, i \in \mathcal{V}^U, m \neq i, \quad (C6)$$

$$z_{min}^U(t) \leq z_m^U(t) \leq z_{max}^U, \forall m \in \mathcal{V}^U \quad (C7)$$

$$\mathbf{C}(t) * \mathcal{S}(t) = \mathcal{S}(t). \quad (C8)$$

The goal of L1 is to maximize transmission performance by optimizing  $\mathbf{Q}$  and  $\mathbf{Z}$  in G2A scenario, where operational constraints are defined by (C1–C7): (C1) UAV velocity  $\mathbf{v}_m(t) \in \mathbb{R}^3$  is capped at  $v_{max}^U$ ; (C2) UAVs are confined within the area of interest with border  $L_E$ ; (C3) each GT is served by at most one UAV on a subchannel; (C4) the number of GTs assigned to each UAV does not exceed available subchannels; (C5) UAV battery energy  $B_m^U(t_{end})$  must remain above  $B_{min}^U$  for safe return at the end slot  $t_{end}$ ; (C6) maintain a safe distance between UAVs; (C7) The flight altitude of UAVs is restricted within the range of  $z_{min}^U(t)$  to  $z_{max}^U$ ; (C8) UAVs can only server GTs within their covering range. Next, the second layer optimization subproblem L2 is formulated as:

$$\mathbb{L}2: \max_{\mathcal{S}, \mathbf{P}, \boldsymbol{\rho}} \frac{D^U(t)}{\beta \hat{E}(t) A^U(t)}, \quad (27)$$

$$\text{s. t. } \sum_{k \in \mathcal{K}} \rho_k \leq 1, \quad (C9)$$

$$0 < P_m^U(t) < P_{max}^U, \quad (C10)$$

$$\sum_{k=1}^K \sum_{l^k \in \mathcal{V}^k} s_m^{l^k}(t) \leq 1, \forall m \in \mathcal{V}^U, \forall k \in \mathcal{K}, \quad (C11)$$

$$\hat{B}_m^U(t+1) = \min \left\{ \hat{B}_m^U(t) + E_m^{Uh}(t), -\hat{E}_m^{Uc}(t), \hat{B}_{max}^U \right\}, \forall m \in \mathcal{V}^U. \quad (C12)$$

L2 focuses on transmission performance improvement by optimizing  $\mathcal{S}$ ,  $\mathbf{P}$ , and  $\boldsymbol{\rho}$  in A2S scenario, where constraints (C9–C12) delineate the feasible operational domain: (C9) Sum of subchannel allocation ratios does not exceed 1; (C10) UAV transmit power is constrained within feasible range  $[0, P_{max}^U]$ ; (C11) each UAV is restricted to connecting to exactly one LEO

SAT at any given time; (C12) UAV energy storage from the harvesting board must not exceed its maximum capacity  $\hat{B}_{max}^U$ .

Next, we demonstrate that the combined solution of subproblems L1 and L2 constitutes the global optimum for  $\mathbb{G}\mathbb{P}$ . For simplicity and without loss of generality, partition the variables into two disjoint sets:  $\mathbf{x} = (\mathbf{Q}, \mathbf{Z})$  and  $\mathbf{y} = (\mathcal{S}, \mathbf{P}, \boldsymbol{\rho})$ . Let  $\mathbf{x}^*$  and  $\mathbf{y}^*$  denote the optimal solutions to L1 and L2, respectively.  $(\mathbf{x}^*, \mathbf{y}^*)$  is optimal for GP under the consistency assumption: at optimality, the individual demands align  $D_m^U(\mathbf{x}^*) = \dot{D}_m^U(\mathbf{y}^*), \forall m \in \mathcal{V}^U$ . This assumption implies that the data collected by each UAV from GTs is identical to that transmitted by each UAV to LEO SATs, ensuring no backlog or resource wastage, achieving supply-demand balance, and meeting the requirements of HHGNN framework optimal solution. Then, we obtain  $\min(D_m^U(\mathbf{x}^*), \dot{D}_m^U(\mathbf{y}^*)) = D_m^U(\mathbf{x}^*) = \dot{D}_m^U(\mathbf{y}^*)$ . Let  $f_{GP}(\mathbf{x}, \mathbf{y})$  denote the objective function of  $\mathbb{G}\mathbb{P}$ , its numerator at  $(\mathbf{x}^*, \mathbf{y}^*)$  simplifies to:

$$\sum_{m=1}^M \min(D_m^U(\mathbf{x}^*), \dot{D}_m^U(\mathbf{y}^*)) = \sum_{m=1}^M D_m^U(\mathbf{x}^*) = D^G(\mathbf{x}^*). \quad (28)$$

Equivalently, (28) equals  $D^U(\mathbf{y}^*)$ . Thus:

$$f_{GP}(\mathbf{x}^*, \mathbf{y}^*) = \frac{D^G(\mathbf{x}^*)}{\beta(E(\mathbf{x}^*) + \hat{E}(\mathbf{y}^*))(A^G(\mathbf{x}^*) + A^U(\mathbf{y}^*))}, \quad (29)$$

$$f_{GP}(\mathbf{x}^*, \mathbf{y}^*) = \frac{D^U(\mathbf{y}^*)}{\beta(E(\mathbf{x}^*) + \hat{E}(\mathbf{y}^*))(A^G(\mathbf{x}^*) + A^U(\mathbf{y}^*))}. \quad (30)$$

For arbitrary  $\mathbf{x}$  and  $\mathbf{y}$ , the min-function implies:

$$\sum_{m=1}^M \min(D_m^U(\mathbf{x}), \dot{D}_m^U(\mathbf{y})) \leq \sum_{m=1}^M D_m^U(\mathbf{x}) = D^G(\mathbf{x}), \quad (31)$$

$$\sum_{m=1}^M \min(D_m^U(\mathbf{x}), \dot{D}_m^U(\mathbf{y})) \leq \sum_{m=1}^M \dot{D}_m^U(\mathbf{y}) = D^U(\mathbf{y}). \quad (32)$$

From (31) and (32), we can obtain:

$$f_{GP}(\mathbf{x}, \mathbf{y}) \leq \frac{D^G(\mathbf{x})}{\beta(E(\mathbf{x}) + \hat{E}(\mathbf{y}))(A^G(\mathbf{x}) + A^U(\mathbf{y}))}, \quad (33)$$

$$f_{GP}(\mathbf{x}, \mathbf{y}) \leq \frac{D^U(\mathbf{y})}{\beta(E(\mathbf{x}) + \hat{E}(\mathbf{y}))(A^G(\mathbf{x}) + A^U(\mathbf{y}))}. \quad (34)$$

By optimality of  $\mathbf{x}^*$  for L1 and  $\mathbf{y}^*$  for L2:  $\frac{D^G(\mathbf{x}^*)}{\beta E(\mathbf{x}^*) A^G(\mathbf{x}^*)} \leq$

$\frac{D^G(\mathbf{x}^*)}{\beta E(\mathbf{x}^*) A^G(\mathbf{x}^*)} = v_1$  and  $\frac{D^U(\mathbf{y}^*)}{\beta \hat{E}(\mathbf{y}^*) A^U(\mathbf{y}^*)} = v_2$ , where  $v_1$  and  $v_2$  are the optimal values of L1 and L2. This implies:  $D^G(\mathbf{x}) \leq v_1 \beta E(\mathbf{x}) A^G(\mathbf{x})$  and  $D^U(\mathbf{y}) \leq v_2 \beta \hat{E}(\mathbf{y}) A^U(\mathbf{y})$ . Substituting into (33) and (34):

$$f_{GP}(\mathbf{x}, \mathbf{y}) \leq \frac{v_1 E(\mathbf{x}) A^G(\mathbf{x})}{(E(\mathbf{x}) + \hat{E}(\mathbf{y}))(A^G(\mathbf{x}) + A^U(\mathbf{y}))}, \quad (35)$$

$$f_{GP}(\mathbf{x}, \mathbf{y}) \leq \frac{v_2 \hat{E}(\mathbf{y}) A^U(\mathbf{y})}{(E(\mathbf{x}) + \hat{E}(\mathbf{y}))(A^G(\mathbf{x}) + A^U(\mathbf{y}))}. \quad (36)$$

From the consistency assumption,  $D^G(\mathbf{x}^*) = D^U(\mathbf{y}^*) \triangleq S$ .

Thus:  $v_1 = \frac{S}{\beta E(\mathbf{x}^*) A^G(\mathbf{x}^*)}$  and  $v_2 = \frac{S}{\beta \hat{E}(\mathbf{y}^*) A^U(\mathbf{y}^*)}$ . According to (29), the right-hand side of (35) at  $(\mathbf{x}^*, \mathbf{y}^*)$  equals:

$$\frac{v_1 E(\mathbf{x}^*) A^G(\mathbf{x}^*)}{(E(\mathbf{x}^*) + \hat{E}(\mathbf{y}^*))(A^G(\mathbf{x}^*) + A^U(\mathbf{y}^*))} = \frac{S}{\beta(E(\mathbf{x}^*) + \hat{E}(\mathbf{y}^*))(A^G(\mathbf{x}^*) + A^U(\mathbf{y}^*))} = f_{GP}(\mathbf{x}^*, \mathbf{y}^*). \quad (37)$$

Similarly, (36) equals  $f_{GP}(\mathbf{x}^*, \mathbf{y}^*)$  at  $(\mathbf{x}^*, \mathbf{y}^*)$  according to (30). Thus, the upper bounds (35) and (36) are tight at  $(\mathbf{x}^*, \mathbf{y}^*)$ . For any  $(\mathbf{x}, \mathbf{y})$ :

$$f_{GP}(\mathbf{x}, \mathbf{y}) \leq \left\{ \frac{v_1 E(\mathbf{x}) A^G(\mathbf{x})}{(E(\mathbf{x}) + \hat{E}(\mathbf{y}))(A^G(\mathbf{x}) + A^U(\mathbf{y}))}, \frac{v_2 \hat{E}(\mathbf{y}) A^U(\mathbf{y})}{(E(\mathbf{x}) + \hat{E}(\mathbf{y}))(A^G(\mathbf{x}) + A^U(\mathbf{y}))} \right\}, \quad (38)$$

where the upper bound equals  $f_{GP}(\mathbf{x}^*, \mathbf{y}^*)$  at  $(\mathbf{x}^*, \mathbf{y}^*)$ , and this value is attainable by the consistency assumptions, i.e.,  $f_{GP}(\mathbf{x}, \mathbf{y}) \leq f_{GP}(\mathbf{x}^*, \mathbf{y}^*)$ . Therefore, the combination of the optimal solutions to  $\mathbb{L}1$  and  $\mathbb{L}2$  is the solution to  $\mathbb{G}\mathbb{P}$ . However, owing to the non-convex nature of MINLP and the gradient descent optimization procedure, the  $\mathbb{G}\mathbb{P}$  solution derived herein is locally optimal. Nevertheless, it satisfies most application requirements at a lower cost compared to the pursuit of global optimality [42].

### C. MDP Formulation

#### 1) MARL MDP of $\mathbb{L}1$

Based on the collaborative communication mode among UAVs, we formulate  $\mathbb{L}1$  as a MARL task where each UAV is treated as an agent to observe environmental states and perform actions. Given the limited computational resources and observed environment states available to each UAV, we adopt a centralized training and distributed execution (CTDE) scheme to optimize the UAV training process. The following is the MDP formulation for a single UAV.

*a) Observation:* The observation of UAV- $m$  in slot  $t$  encompasses its own features as well as those of surrounding GTs and UAVs located within its sensing range, described by associated neighborhood sets  $\mathcal{N}_m^G(t) = \{n | g_{n,m}(t) = 1, \forall n \in \mathcal{V}^G\}$  and  $\mathcal{N}_m^U(t) = \{i | u_{i,m}(t) = 1, \forall i \in \mathcal{V}^U\}$ . Therefore, the observation of UAV- $m$  in slot  $t$  is

$$\sigma_m^t = \langle \{ \mathbf{q}_m^U(t), B_m^U(t), \{\mathbf{q}_i^U(t), B_i^U(t)\}_{i \in \mathcal{N}_m^U(t)}, \{\mathbf{q}_n^G(t), B_n^G(t), \epsilon_n(t), \mathbf{a}_n^G(t), \widehat{D}_n^G(t)\}_{n \in \mathcal{N}_m^G(t)} \rangle. \quad (39)$$

The attributes of UAVs include position and battery level, while those of GTs incorporate these two elements along with GT type, AoI, and cumulative data transmission volume, enabling UAVs to optimize trajectories and WET decision, accordingly. The observation length at each UAV varies across time slots and differs among UAVs, motivating the use of GNN-based solution.

*b) Action:* In each slot, each UAV- $m$  agent outputs UAV- $m$ 's velocity vector and WET decision, i.e.,  $\mathbf{a}_m^t = \{\mathbf{V}_m(t), Z_m(t)\}$ , and  $\mathbf{q}_m^U(t+1)$  can be easily calculated based on UAV- $m$ 's three-dimensional velocity vector  $\mathbf{V}_m(t) = \{V_m^X(t), V_m^Y(t), V_m^Z(t)\}$ . Given that  $\mathbf{V}_m(t)$  is continuous while  $Z_m(t)$  are discrete, we employ neural networks with continuous action outputs and quantize the interval  $[-1, 1]$  corresponding to  $Z_m(t)$  for more precise trajectory optimization. Specifically, positive values map to  $Z_m(t) = 1$  and negative values to  $Z_m(t) = 0$ .

*c) Reward:* Since UAVs can perform two behaviors, i.e., WDC and WET, we set up separate reward formulas for them. The reward for UAV- $m$  regarding WDC in slot  $t$  is

$$r_m^{WDC}(t) = \sum_{n=1}^N a_n^G(t) W^U \log(1 + \gamma_{n,m}(t)) \tau. \quad (40)$$

(40) Ensure that UAVs prioritize serving GTs with high AoI  $a_n^G(t)$  while considering data collection. Accordingly, the reward for UAV- $m$  regarding WET in slot  $t$  is

$$r_m^{WET}(t) = \sum_{n=1}^N a_n^G(t) \frac{E_n^{GH}(t) P_E^U Z_m(t) h_{n,m}(t)}{\sum_{m=1}^M P_E^U Z_m(t) h_{n,m}(t)}. \quad (41)$$

Since the energy harvesting contribution of each UAV to each GT varies, (41) requires calculating the contribution ratio

$\frac{P_E^U Z_m(t) h_{n,m}(t)}{\sum_{m=1}^M P_E^U Z_m(t) h_{n,m}(t)}$  of UAV- $m$ . Meanwhile, priority in energy provision is given to GTs with high AoI to ensure that they have sufficient energy to transmit data promptly. Combining (40) and (41), the total reward formula for UAV- $m$  is obtained as

$$r_m^t = \frac{\zeta_1 r_m^{WDC}(t) + \zeta_2 r_m^{WET}(t)}{A^G(t) E_m^{UC}(t)}, \quad (42)$$

where  $\zeta_1$  and  $\zeta_2$  are non-negative coefficients to ensure that the distinct rewards maintain identical or comparable magnitudes. The rewards are divided by the total GT AoI  $A^G(t)$  and UAV- $m$ 's energy consumption  $E_m^{UC}(t)$  to enable rewards to objectively reflect UAVs' contribution to transmission under different transmission environments, while driving UAVs to improve energy efficiency. Furthermore, no penalty terms for constraint violations are added because invalid actions are masked, which will be detailed in Section V.

#### 2) SARL MDP of $\mathbb{L}2$

To avoid contention between LEO SATs for subchannels and additional communication delay caused by redundant collaborative communication between agents in A2S scenarios, we formulate  $\mathbb{L}2$  as a SARL task. Specifically, the steps are as follows: arbitrarily select a LEO and deploy an agent model as the central controller in each of its SATs; during the training phase, when the coverage of the currently serving SAT is about to exclude the target area, the SAT transfers its agent parameters to the successor SAT, with continuous iteration; during the execution phase, since agent models no longer update, the agent parameters in all SATs are identical, eliminating the need for parameter transmission. The following is the MDP formulation.

*a) State:* The SAT agent's state space comprises UAVs' AoI, transmission task amount, energy harvesting board's battery level, UAV-SAT channel gain, and LEO SAT location  $\mathbf{q}_{ik}^S(t) = (x_{ik}^S(t), y_{ik}^S(t), z_{ik}^S(t))$ , which can be represented as

$$\mathcal{S}^t = \langle \{ \mathbf{a}_m^U(t) \}; \{ \widehat{D}_m^U(t) \}; \{ \widehat{B}_m^U(t) \}; \{ \mathbf{a}_m^L(t) \}; \{ \mathbf{q}_{ik}^S(t) \} \rangle_{\forall m \in \mathcal{V}^U, l, k \in \mathcal{V}^k, \forall k \in \mathcal{K}}. \quad (43)$$

*b) Action:* In each slot, the SAT agent makes decisions on UAV-LEO scheduling, UAV transmit power control, and LEO's subchannel allocation, with its action space defined as follows:

$$\mathcal{A}^t = \langle \{ \mathbf{s}_m^L(t) \}; \{ P_m^U(t) \}; \{ \rho_k(t) \} \rangle_{\forall m \in \mathcal{V}^U, l, k \in \mathcal{V}^k, \forall k \in \mathcal{K}}. \quad (44)$$

*c) Reward:* To enhance the actual data transmission volume of UAVs while reducing their AoI and energy consumption, the reward function is designed as follows:

$$\mathcal{R}^t = \sum_{m=1}^M \frac{a_m^U(t) \widehat{D}_m^U(t)}{A^U(t) E_m^{UC}(t)}. \quad (45)$$

## V. NEURAL NETWORKS AND ALGORITHMS DESIGN

In this section, we define diverse GNN layers, construct the network architecture of HHGNN, design corresponding algorithms, and finally analyze the algorithms' time complexity.

### A. Neural Networks Design

*1) Heterogeneous Graphs Construction:* As shown in Fig. 2, we adopt a heterogeneous graph  $\mathcal{G} = (\mathcal{V}, \mathcal{E})$  to characterize the device vertices of GTs, UAVs, and LEO SATs, as well as their mutual relations, where  $\mathcal{V} = \mathcal{V}^G \cup \mathcal{V}^U \cup \{\mathcal{V}^k\}_{\forall k \in \mathcal{K}}$ . The

relations in  $\mathcal{E}$  include: sensing: (GT, sensed-by, UAV), (UAV, sensed-by, UAV), (UAV, sensed-by, SAT), and (SAT, sensed-by, SAT); exchange: (UAV, exchange-with, UAV) and (SAT, exchange-with, SAT); service: (GT, transmit-to, UAV), (UAV, power, GT), and (UAV, transmit-to, SAT). A sensing relation  $(i, j)$  exists if device  $i$  is within  $j$ 's sensing or coverage range. An exchange relation exists if UAVs are mutually within each other's sensing range. A service relation  $(i, j)$  exists on the premise that device  $i$  is within  $j$ 's coverage range. The sensing or exchange relations between SATs exist only if they are currently covering the target area in each orbit. Additionally, since GTs harvest all RF power from UAVs and perform non-linear power transformation via (8), UAVs conducting WET have service relations with all E-GTs. It is noted that Fig. 2 reflects the actual inter-device relations. In GNNs, only UAVs or SATs serve as destination vertices for state information transmission (rather than GTs), as this aligns with real-world communication scenarios where high-load tasks are not processed on GTs with limited computational resources. As observed from Fig. 2, the overall heterogeneous graph comprises multiple local sensing and exchange subgraphs. Next, we define GSL and GEL to manage sensing and exchange features, and define GML to handle unavailable actions output by the GNN.

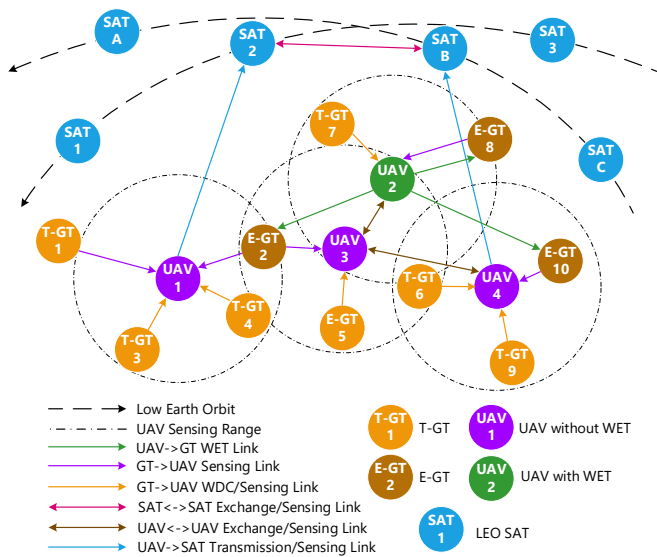


Fig. 2. Graph representation of PDPCIN topology.

2) *Graph Sensing Layer*: Most existing works encode features by a multi-layer perceptron (MLP), which can only process intrinsic vertex features and fail to effectively handle graph-structured features due to their inability to aggregate neighbor information. In contrast, graph neural networks (GNNs) capture topological relations and vertex dependencies via message passing, making them more suitable for the time-varying concatenated communication scenario in this study. Given the limited expressive power of traditional graph attention (GAT) with static attention mechanisms, we adopt strictly more expressive GATv2 [43]. Since the G2A scenario observations include GTs and UAVs, while the A2S scenario states involve UAVs and SATs, we employ two GATv2 in each GSL to weight information from different source vertices at

each destination vertex. The weight coefficient for each GT, UAV, and SAT is obtained as

$$\left\{ \begin{aligned} \alpha_{in}^G &= \frac{\exp(\text{LeakyReLU}(\mathbf{a}_G^T(\mathbf{W}_{agent}\mathbf{h}_i \parallel \mathbf{W}^G \mathbf{v}_i^G(t))))}{\sum_{l \in \mathcal{N}_m^G(t)} \exp(\text{LeakyReLU}(\mathbf{a}_G^T(\mathbf{W}_{agent}\mathbf{h}_i \parallel \mathbf{W}^G \mathbf{v}_l^G(t))))} \\ \alpha_{im}^U &= \frac{\exp(\text{LeakyReLU}(\mathbf{a}_U^T(\mathbf{W}_{agent}\mathbf{h}_i \parallel \mathbf{W}^U \mathbf{v}_m^U(t))))}{\sum_{l \in \mathcal{N}_m^U(t)} \exp(\text{LeakyReLU}(\mathbf{a}_U^T(\mathbf{W}_{agent}\mathbf{h}_i \parallel \mathbf{W}^U \mathbf{v}_l^U(t))))}, \\ \alpha_{ilk}^S &= \frac{\exp(\text{LeakyReLU}(\mathbf{a}_S^T(\mathbf{W}_{agent}\mathbf{h}_i \parallel \mathbf{W}^S \mathbf{v}_{lk}^S(t))))}{\sum_{l \in \mathcal{N}^S(t)} \exp(\text{LeakyReLU}(\mathbf{a}_S^T(\mathbf{W}_{agent}\mathbf{h}_i \parallel \mathbf{W}^S \mathbf{v}_l^S(t))))} \end{aligned} \right. \quad (46)$$

where  $\mathbf{h}_i$  is agent- $i$ 's current features,  $\mathcal{N}^S(t)$  is the set of SATs currently covering the target area in each orbit,  $\mathbf{v}_n^G(t)$ ,  $\mathbf{v}_m^U(t)$ ,  $\mathbf{v}_{lk}^S(t)$  is the initial features of GT- $n$ , UAV- $m$ , and SAT- $l^k$ ,  $\mathbf{a}^T$  is  $\mathbf{a}$ 's transpose matrix,  $\parallel$  represents concatenation, and  $\mathbf{W}_{agent}$ ,  $\mathbf{W}^G$ ,  $\mathbf{W}^U$ ,  $\mathbf{W}^S$ ,  $\mathbf{a}_G$ ,  $\mathbf{a}_U$ , and  $\mathbf{a}_S$  are trainable vectors. The updated features, derived as the weighted sum of features from all incident neighbors, is calculated through

$$\left\{ \begin{aligned} \mathbf{h}_i^G &:= \sigma \left( \sum_{l \in \mathcal{N}_i^G(t)} \alpha_{in}^G \mathbf{W}^G \mathbf{v}_l^G(t) \right) \\ \mathbf{h}_i^U &:= \sigma \left( \sum_{l \in \mathcal{N}_i^U(t)} \alpha_{im}^U \mathbf{W}^U \mathbf{v}_l^U(t) \right), \\ \mathbf{h}_i^S &:= \sigma \left( \sum_{l \in \mathcal{N}^S(t)} \alpha_{ilk}^S \mathbf{W}^S \mathbf{v}_l^S(t) \right) \end{aligned} \right. \quad (47)$$

where  $\sigma$  is the sigmoid activation function. To enhance training stability, multi-head attention is applied by independently deploying multiple attention mechanisms, whose outputs are concatenated. The observation embedding for GTs is computed as  $\mathbf{h}_i^G := \parallel_{a=1}^A \sigma \left( \sum_{l \in \mathcal{N}_i^G(t)} \alpha_{in}^a \mathbf{W}_a^G \mathbf{v}_l^G(t) \right)$  where  $A$  is the number of heads. The embeddings of  $\mathbf{h}_i^U$  and  $\mathbf{h}_i^S$  can be obtained similarly. These are then fused via an MLP to produce the final vertex representation  $\mathbf{h}_i$ . The self-attention mechanism enables GATv2 to selectively process inputs from dynamically varying sets of GTs/UAVs/SATs based on relevance. The heterogeneous GATv2 layer dedicated to features sensing is termed graph sensing layer (GSL).

3) *Graph Exchange Layer*: While GAT performs well in sensing features processing, (44) reliance on exchanging high-dimensional hidden features makes it inefficient for inter-agent exchange. As the feature dimension increases, so does the exchange cost. To reduce backhaul burden, feature compression is required. Existing methods either treat discrete messages as agent actions, requiring auxiliary reinforcement learning due to the absence of gradients, or transmit continuous messages with quantization noise [44].

In this work, we adopt a differentiable discrete messaging scheme, and define the GEL with an encoder-decoder architecture. Specifically, edge update function  $\rho_{exc}^e$ , parameterized by MLP  $N_{enc}$ , works as an encoder and transforms UAV/SAT features into logits over a discrete symbol set, which are subsequently utilized to select symbols for transmission. To enable backpropagation, we use the Gumbel-Softmax trick, which reparameterizes categorical sampling into a differentiable form. Gumbel-Softmax approximates a one-hot vector as temperature  $\tau^e \rightarrow 0$ , allowing gradient flow during training, and hard symbols are sampled directly during inference [29]. In detail, function  $\rho_{exc}^e$  first aggregates discrete messages via a max-pooling operation at the receiver side, then  $N_{dec}$  decodes the outcome. Recurrent neural

network (RNN), working as vertex update function, is used to take current vertex features and aggregated information from neighboring agents. Thus, the update of UAV features is expressed as

$$\mathbf{h}_i := \text{RNN} \left[ \mathbf{h}_i \parallel N_{dec} \left( \max_{l \in \mathcal{N}_m^U(t)} \left( \text{GS}(N_{enc}(\mathbf{h}_l)) \right) \right) \right], \quad (48)$$

where GS is abbreviation for Gumbel-Softmax. SAT features can be processed in the same way.

4) *Graph Mask Layer*: As indicated by constraints (C1-C12), the optimization problems are subject to multiple restrictions. To ensure neural network outputs comply with these constraints, two common strategies, soft-constraint and hard-constraint, are available. Soft-constraint discourages invalid actions by assigning low or negative rewards but cannot fully prevent them, while hard-constraint preemptively masks invalid actions, ensuring feasibility but requiring prior knowledge of all infeasible actions. Since some constraints in our scenario are only verifiable post-decision, hard constraints are inapplicable. Therefore, we propose a new constraint method, GML, based on the characteristics of GNN structure. It determines the action vector  $\mathbf{a}$  based on the graph features  $\mathbf{h}_i$ .

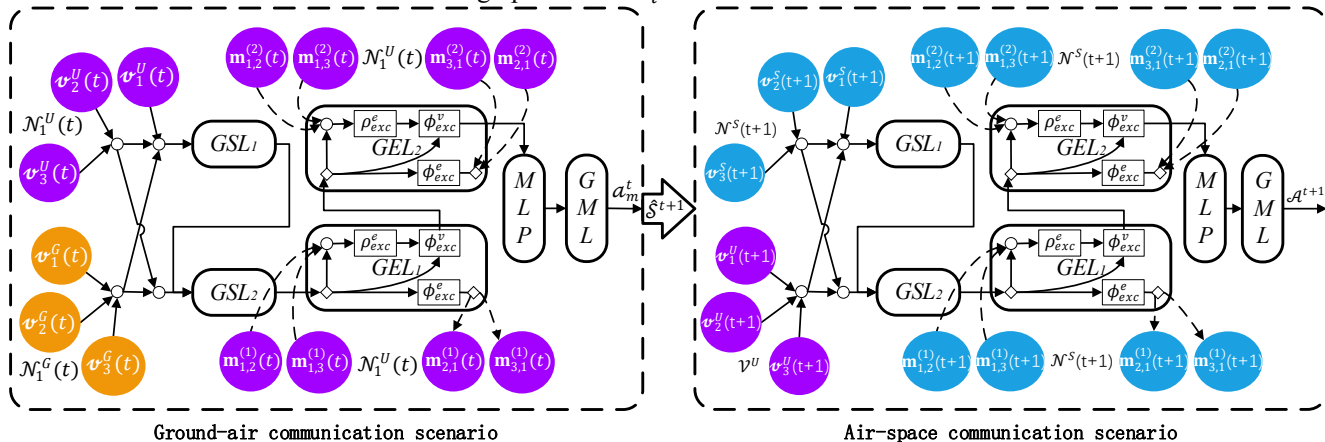


Fig. 3. HHGNN architecture with G3Ms. Sensing, exchange, and masking correspond to agent-1 in G2A and A2S scenario.

5) *Concatenated Structure*: As show in Fig. 3, multiple layers are stacked to enhance model capacity, forming a concatenated structure, where  $\mathbf{m}_{i,j}^{(l)}(t)$  denotes the message of neighbor vertex- $j$  updated by the  $l$ -th GEL after processing via GSLs,  $\phi_{exc}^v$  and  $\phi_{exc}^e$  are vertex update and edge update functions, and the updated state  $\mathcal{S}^{t+1} = \langle \{a_m^U(t+1)\}; \{\bar{D}_m^U(t+1)\}; \{\bar{B}_m^U(t+1)\}_{\forall m \in \mathcal{V}} \rangle$  after all UAVs execute decisions in slot  $t$  within the G2A scenario constitutes a part of the MDP's state  $\mathcal{S}^{t+1}$  in A2S scenario. Let  $L_S$  and  $L_E$  denote the number of GSL and GEL, respectively. In slot  $t$ , agent- $i$ 's features after  $l$ -th update are denoted  $\mathbf{h}_i^{(l)}(t)$ , where  $0 \leq l \leq L_S + L_E$ . The neural network model incorporating GSL, GEL, and GML is named G3M for briefness. Fig. 3 only shows one G3M in G2A scenario, which involves multiple G3Ms in fact, with each UAV having a G3M as an agent. Taking G2A scenario as an example, during forward propagation, GSL update only destination vertices, leaving source vertex features unchanged. Thus, when agent- $i$  is the destination, its feature evolves as  $\mathbf{h}_i^{(l)}(t)$ ; when it is a source (i.e., observed by others), its features remain  $\mathbf{h}_i^{(0)}(t)$ . After applying  $L_S$  GSL locally, agent- $i$  obtains hidden features  $\mathbf{h}_i^{(L_S)}(t)$ , which is further

If actions are feasible, they are used directly. Otherwise, use smooth-mask mechanism to adjust the distribution of actions, ensuring actions align with the graph structure and remain valid. The modification of  $\mathbf{a}$  is

$$\mathbf{a}' = \begin{cases} \mathbf{a}, & \text{if } f_G(\mathbf{h}_i, \mathbf{a}) \in \Omega_G \\ f_{\Omega_G}(\mathcal{G}_\theta(\mathbf{a}) \circ (\boldsymbol{\mu}_\theta + \boldsymbol{\sigma}_\theta + \varepsilon)), & \text{otherwise} \end{cases}, \quad (49)$$

where  $\varepsilon$  is noise,  $f_G(\cdot)$  is global risk assessment function evaluating whether the state-action pair is within the feasible domain  $\Omega_G$ ,  $\boldsymbol{\mu}_\theta$  and  $\boldsymbol{\sigma}_\theta$  are the mean and standard deviation vector of  $\mathbf{a}$  output by MLP,  $\mathcal{G}_\theta(\cdot)$  is a smooth function used to dynamically adjust the feasibility weights of each dimension of the action,  $\circ$  is element-wise multiplication combining the GNN's smooth vector with the original action distribution to smooth the discrepancy between infeasible and normal actions,  $f_{\Omega_G}(\cdot)$  is the projection operator to fine-tune infeasible actions via noise addition to keep them within feasible domain  $\Omega_G$ . The proposed method fully blocks infeasible actions while balancing the rationality of corrected actions to maximally preserve their original features.

refined through  $L_E$  GEL via message exchange with neighbors, i.e.,  $\mathcal{N}_m^U$  or  $\mathcal{N}^S(t)$ . If an agent has no neighbors, a zero vector is used as the aggregated message. Notably, features from neighbors contain their own features in GSL, while integrated messages from neighbors include not only their own feature information but also information received from other vertices and some historical information in GEL.

## B. Algorithms Design

1) *Training Process of G3M*:  $\mathbb{L}1$  and  $\mathbb{L}2$  are addressed using CTDE-MARL and SARL, respectively, which rely on environmental interactions for training through dynamic state-action-reward data collection. Both aim to maximize cumulative rewards via classic RL frameworks (e.g., policy gradient and value function estimation), following an iterative data sampling-evaluation-optimization loop to adapt strategies through environmental feedback. Therefore, taking the G2A scenario as an example, we introduce the training process of G3M. For the training procedures in the A2S scenario, the number of agents can be set to 1, and the corresponding environmental parameters should be replaced accordingly. The following are the specific steps of Algorithm 1.

**Algorithm 1:** Training Process of G3M

---

```

1: for episode from 1 to  $N^{ep}$  do
2:   Reset the environment and devices states;
3:   while  $t \leq T$  do
4:     for all agent  $i \in \mathcal{V}^U$  do
5:       Get access to  $\mathcal{N}_m^G(t)$  and  $\mathcal{N}_m^U(t)$  to receive  $\sigma_i^t$ ;
6:       for  $l$  from 1 to  $L_S$  do
7:         Apply GSL on local graph and obtain features  $\mathbf{h}_i^{(l)}(t)$ ;
8:       end for
9:       for  $l$  from 1 to  $L_E$  do
10:        Encode and send messages  $\mathbf{m}_{ij}^{(l)}(t)$  to  $j \in \mathcal{N}_m^U(t)$  via GEL;
11:        Decode and aggregate messages  $\mathbf{m}_{ij}^{(l)}(t)$  from  $j \in \mathcal{N}_m^U(t)$ 
            with hidden state  $\mathbf{z}_i^t$  via GEL, and obtain  $\mathbf{z}_i^{t+1}$ ;
12:       end for
13:       Obtain  $\mathbf{a}_i^t$  via GML, receive reward  $r_i^t$ , and observe  $\sigma_i^{t+1}$ ;
14:     end for
15:     Store  $\{\{\sigma_i^t, \mathbf{z}_i^t, \mathbf{a}_i^t, r_i^t, \sigma_i^{t+1}, \mathbf{z}_i^{t+1}\}_{i \in \mathcal{V}^U}\}$  into replay memory  $\mathcal{D}$ ;
16:     If  $|\mathcal{D}| > |\mathcal{B}|$  then
17:       Draw a batch of samples  $\mathcal{B}$  and update model weights  $\theta$  by
           classic loss function;
18:     End if
19:     Update weights of target network  $\hat{\theta}$  by  $\hat{\theta} = \xi\theta + (1 - \xi)\hat{\theta}$ ;
20:      $t \leftarrow t + 1$ ;
21:   End while
22: End for

```

---

Each agent's computational complexity is determined by the forward computation of the trained network, which comprises four components: GSL for sensing observation encoding, GEL for multi-vertex exchange, MLP for feature forward propagation, and GML for unavailable action masking. Their corresponding time complexities are  $O_1 = \mathcal{O}(L_S(AN_{nei}d_{in}d_{out} + ANd_{out}))$ ,  $O_2 = \mathcal{O}(L_E N_{nei}d_{in}d_{out})$ ,  $O_3 = \mathcal{O}(\sum_{j=2}^{L_A} N_{j-1}' \cdot N_j')$  and  $O_4 = \mathcal{O}(dim(\mathbf{a}))$  [18], [45], where  $N_{nei}$  is the number of neighbors,  $d_{in}$  and  $d_{out}$  are input and output feature dimensions,  $L_A$  and  $N_j'$  are the number of fully connected (FC) layers of MLP and the number of neurons in the  $j$ -th layer, and  $dim(\mathbf{a})$  is the dimension of action  $\mathbf{a}$ . Thus, the total time complexity of G3M is approximated by  $O^{G3M} = \sum_{i=1}^4 O_i N^{ep} T$ . Since complexity scales with the number of neighbors, neurons, FC layers, and action dimension, the model flexibly accommodates varying environmental carrying capacity and communication service demand.

2) *S-LSDO Algorithm under HHGNN Architecture:* Aiming to reveal the dynamic balance mechanism between satellite deployment density, communication timeliness, and resource efficiency, we investigate the relation between SAT density of single-LEO, AoI, and spectrum efficiency. Increasing SAT density shortens the service interval for UAV and reduces S-AoI proportion, but elevates deployment and maintenance costs while intensifying inter-satellite interference and channel competition. Conversely, lower density mitigates interference and enhances spectrum efficiency but may increase S-AoI proportion due to SATs' insufficient coverage. Optimizing deployment density enables collaborative optimization of spectrum efficiency and AoI, providing theoretical foundations for LEO satellite network design. Therefore, we propose the S-LSDO algorithm under HHGNN architecture, as illustrated in Algorithm 2. While engaged in solving  $\mathbb{G}\mathbb{P}$ , this algorithm additionally undertakes the task of determining the appropriate the number of single-LEO SATs, using variable-bound binary search-based iterative optimization mechanism.

**Algorithm 2:** S-LSDO Algorithm under HHGNN Architecture

---

```

Input: S-AoI proportion range  $\partial^S$ , number of subchannels  $Y^S$ ;
Output: the number of SATs in a single-LEO  $L^S$ ;
1: Dispatch UAVs to the post-disaster area and allocate a G3M to each of
   them forming model set  $\mathcal{C}$ ;
2: Find the SAT in each LEO currently providing services and label their
   successors as the first LEO satellite in each LEO;
3: Build the SAT set  $\mathcal{V}^k, \forall k \in \mathcal{K}$  of each LEO based on SAT motion
   patterns and allocate a G3M  $m$  to them;
4: Run Algorithm 1 to train model set  $\mathcal{C}$  for solving subproblem  $\mathbb{L}1$ ;
5: Initialize  $L^{max}$  with an empirical large value and  $L^{min}$  an empirical small
   value;
6: repeat
7:    $N^S \leftarrow L^{min} + (L^{max} + L^{min})/2$ ;
8:   Run Algorithm 1 using  $\delta^{t+1}$  (generated by model set  $\mathcal{C}$ ) to train
       model  $m$  for solving subproblem  $\mathbb{L}2$ ;
9:   Invoke model  $m$  to get S-AoI proportion  $\partial$ ;
10:  if  $\partial > \partial^S$  then
11:     $low \leftarrow L^S + 1$ ;
12:  else if  $\partial < \partial^S$  then
13:     $high \leftarrow L^S - 1$ ;
14:  end if
15: until  $\partial$  in  $\partial^S$ 
16: return  $L^S$ ;

```

---

The time complexity of Algorithm 2, composed of the number of searches and  $\mathbb{L}2$ 's G3M iterative training, is expressed as  $O' = \mathcal{O}(\log(L^{max} - L^{min}) * O^{G3M})$ . The efficiency of the search stems from its logarithmic time complexity, making it suitable for fast retrieval in large-scale SATs. Suitable value of  $L^{max}$  and  $L^{min}$  will enhance the algorithm's efficiency. For this reason, we present the derivation of S-AoI proportion expected value in Section VI, which is intended to facilitate the selection of  $L^{max}$  and  $L^{min}$ .

## VI. SIMULATION EXPERIMENTS

In this section, we first configure the experimental environment and key parameters, then present the relevant comparison schemes, subsequently conduct an analysis of the experimental results, and ultimately derive the expected value expressions for AoI and S-AoI proportion.

### A. Simulation Setups

Four UAVs are deployed to a 1.5 km  $\times$  1.5 km post-disaster area with 9 GTs randomly positioned. UAVs harvest up to 80% of their maximum energy harvesting panel capacity per time slot. Four LEO with a radius of 6921 km cover the area, referring to the coverage model in [22] and [46].

TABLE II  
SIMULATION PARAMETERS

Parameter	Value	Parameter	Value
$N_0$	-174 dBm/Hz	$W^U, W^S$	1 MHz, 1 MHz
$z_{min}^U(t), z_{max}^U(t)$	60 m, 120 m	$Y^U, Y^S$	2, 10-40
$\alpha_r, \alpha_n, a, b$	3, 5, 12.08, 0.11	$P_r^G, P_r^E, P_r^U$	10 mW, 1 W, 10 mW
$P_{sen}, P_{sat}$	-10 dBm, 7 dBm	$B_E, B_I, P_{max}^U$	0.01 J, 0.5 J, 1 W
$B_{max}^G, B_{max}^U, \hat{B}_{max}^U$	1 J, 500-2000 J, 10 J	$d_{min}, \tau$	10 m, 1 s
$O_S^G, O_S^U, O_C^U$	400 m, 400 m, 200 m	$v_{max}^U, V^S$	30 m/s, 7.59 km/s
$G_m^k/T_N, \lambda_m^k$	34 dB/K, 8 dB	$\mu_r, \sigma_r^2$	-2.6 dB, 1.63 dB
$\kappa$	$1.38 \times 10^{-23}$ J/m	$d_E, h_k$	6371 km, 550 km

Each LEO's SAT configuration refers to Starlink Block v1.5, where SATs' number, altitude, and velocity are 22, 550 km, and 7.59 km/s, respectively. In each G3M, the numbers of GSL and GEL are set to  $L_S = 2$  and  $L_E = 2$ , using one GML to handle unavailable actions, with 4 attention heads in each GSL.

To further explore scheme performance in air-ground environments, an additional identical post-disaster area is added, deploying another 4 UAVs, creating an 8-UAV high-load A2S scenario to highlight performance differences and robustness. Other key parameters are listed in Table II.

### B. Comparison Schemes

To further validate the effectiveness of our schemes IS-UAV and DMLA, and investigate the impact of optimization factors on the optimization problems, we develop four comparison schemes for  $\mathbb{L}1$  and  $\mathbb{L}2$ , respectively.

1)  $\mathbb{L}1$  Comparison Schemes: a) *DC-UAV*: This scheme is proposed in [18], where UAVs dynamically determine whether to perform WET or WDC. b) *TD-UAV*: This scheme, proposed in [12], divides UAVs into two teams: one solely responsible for WET and the other exclusively for WDC. c) *PD-UAV*: This scheme adopts the classic time phase division, where all UAVs perform WET before time slot  $t'$  and WDC thereafter, with  $t'$  determined via a greedy algorithm. d) *O-UAV*: This scheme deploys trajectory-fixed opportunistic UAVs following [47], with WDC/WET decisions operating under the PD-UAV strategy.

2)  $\mathbb{L}2$  Comparison Schemes: a) *Frequency Division Multiple Access with Power Control (FDPC)*: Neural networks optimize UAV-LEO scheduling, subchannel allocation, and UAV power control, with UAVs employing FDMA on their own dedicated subchannels. b) *Time Division Multiple Access with Fixed Control (TDFP)*: This scheme partitions each time slot into equal segments based on the number of UAVs, where each UAV occupies a segment and transmits data to the nearest LEO SAT among all LEOs' SAT with fixed power across all subchannels. c) *Frequency and Time Division Multiple Access with Power Control (FTPC)*: Unlike FDPC, this scheme uses FDMA for UAVs connected to different LEO SATs and TDMA for those connected to the same LEO SAT. d) *Uniform Allocation with Fixed Power (UAFP)*: Subchannels are uniformly allocated to each LEO, with an equal number of fixed-power UAVs accessing each LEO's SATs.

3)  $\mathbb{G}P$  Comparison Schemes: Our approach to solving  $\mathbb{G}P$  iteratively employs solutions to  $\mathbb{L}1$  and  $\mathbb{L}2$ , hence termed IS-UAV-DMLA. Moreover, given the superior performance of IS-UAV over  $\mathbb{L}1$  comparison schemes (as demonstrated later), the comparative analysis for  $\mathbb{G}P$  and single-LEO SAT density optimization integrates IS-UAV with  $\mathbb{L}2$  comparison schemes, denoted as IS-UAV-FDPC, IS-UAV-TDFP, IS-UAV-FTPC, and IS-UAV-UAFP. In addition, we define two metrics to further evaluate transmission performance, i.e., energy transfer efficiency (ETE), which is the ratio of data transmission volume to energy consumption per unit time, and spectrum transmission efficiency (STE), which is the ratio of data transmission volume to bandwidth per unit time.

### C. Simulation Results

#### 1) Performance Comparison of Different Schemes to $\mathbb{L}1$

Fig. 4 (a) and Fig. 4 (b) illustrate the convergence of data transmission and AoI for various schemes during training. The proposed IS-UAV scheme demonstrates the best performance with minimal fluctuations, followed by DC-UAV. These two

schemes exhibit greater flexibility in WDC/WET decision-making, enabling more adaptive state-action pair matching and superior convergence. PD-UAV and TD-UAV show similar performance but with larger fluctuations. Both adopt static partitioning for WDC/WET decisions (either in device or time dimensions), while the longer time span of TD-UAV introduces higher system instability, leading to pronounced training variations. O-UAV, leveraging idle resources from other UAVs for communication without DRL-based decision-making, remains unaffected by training in transmission performance.

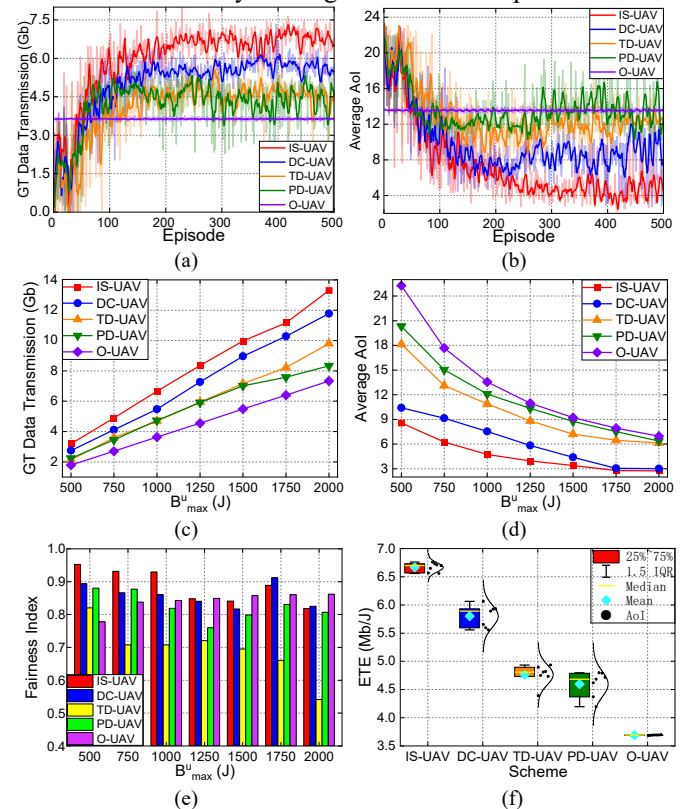


Fig. 4. Performance comparison of different schemes to  $\mathbb{L}1$  under different UAV battery capacities.

Fig. 4 (c), 4 (d), and 4 (e) compare the average data transmission volume per UAV task cycle, AoI, and Fairness across schemes under different UAV battery capacities  $B_{max}^U$ . Overall, as  $B_{max}^U$  increases, all schemes show improved transmission capacity due to more available energy for services. However, Fig. 4(d) reveals this trend slows down, and AoI gaps between schemes narrow, as energy saturation diminishes the impact of each scheme's unique WDC/WET decision-making mechanism, with spectral bandwidth and path planning becoming primary constraints. Fig. 4(e) shows a slight downward trend in the Fairness of each scheme, attributed to the heterogeneity in GTs' states and transmission requirements, which leads to non-absolute equity in UAV services. Nevertheless, such fairness remains within an acceptable range.

Further comparative analysis of the schemes reveals that the baseline O-UAV performs worst but approaches PD-UAV and TD-UAV performance when  $B_{max}^U$  is abundant. TD-UAV and PD-UAV underperform IS-UAV and DC-UAV due to static resource partitioning: The team-based execution of WDC or WET by TD-UAVs leads to uneven load distribution between the two UAV teams, and fails to dynamically adjust the team sizes according to real-time requirements for energy

replenishment or task transmission., while PD-UAV's phased execution of WET and WDC results in significant data backlog in the early stage, causing a sharp increase in AoI and affecting information timeliness, explaining its worse AoI performance than TD-UAV. IS-UAV and DC-UAV dynamically allocate resources for WDC/WET, avoiding idle or busy team issues and eliminating AoI surges from pre-charging GTs. The superior performance of IS-UAV over DC-UAV stems from the latter's slot-level state switching, which inherently operates in a serial processing mode, leading to time resource wastage. In practical scenarios, task switching incurs non-negligible delays (e.g., reconfiguring communication parameters), prolonging the overall task completion time and failing to simultaneously address the dual urgent needs of data transmission and energy replenishment from GTs in post-disaster areas—such as when a GT with critical battery levels needs to transmit high-priority data. By contrast, IS-UAV's parallel processing enables synchronous WDC and WET within the same time window, ensuring both data communication continuity and energy sustainability for GTs. This eliminates device power-offs or data loss caused by time-division waiting. Ideally, IS-UAV can reduce task completion time to less than 50% of traditional time-division schemes, making it highly adaptive to post-disaster communication scenarios.

Finally, Fig. 4 (f) shows the statistically analyzed ETE for each scheme across all UAV battery capacities  $B_{max}^U$ . It can be observed that IS-UAV demonstrates the best overall performance, while O-UAV exhibits the worst yet most stable performance. However, by leveraging idle resources to provide additional communication services, O-UAV essentially achieves further enhancement of ETE. Due to phased fixed WDC/WET mode, PD-UAV fails to address real-time environmental demands, leading to the most significant fluctuations in its ETE performance.

## 2) Performance Comparison of Different Solutions to $\mathbb{L}2$

Fig. 5 (a) and Fig. 5 (b) depict the average data transmission volume per slot and STE of each scheme under different numbers of subchannels. DMLA demonstrates the best transmission performance, verifying that NOMA achieves higher channel utilization efficiency than other access methods. FTPC outperforms FDPC because the former employs fine-grained time division, adapting better to time-varying environments while avoiding uncontrollable interference from simultaneous signal transmissions. TDFP and UAFP exhibit nearly identical performance as both essentially adopt equal resource allocation, but TDFP slightly surpasses UAFP since each UAV in TDFP connects to the nearest SAT among all LEOs, optimizing channel gain, whereas UAFP evenly distributes to the nearest SATs of each LEO, resulting in suboptimal channel gain. However, TDFP's single SAT access causes load imbalance among SATs, while EDFF ensures the most balanced SAT load across all schemes. Notably, the STE of all schemes decreases with increasing subchannels: when the transmission task volume is fixed, abundant subchannels and limited UAV energy storage reduce the average power allocated to each channel, decreasing channel bandwidth utilization efficiency. DMLA and FTPC show more pronounced STE decline to balance ETE.

Fig. 5 (c) and Fig. 5 (d) illustrate the average UAV energy consumption per slot and ETE under different subchannel numbers. Initially, when subchannels are scarce, DMLA's UAV energy consumption far exceeds other methods, with low ETE, because NOMA's channel sharing allows UAVs to allocate power across multiple subchannels, and power control increases transmit power to meet transmission demands under resource shortage. However, the ETE of DMLA and FTPC rises with more subchannels. Leveraging their superior transmission capabilities, the two schemes can reduce transmit power appropriately under sufficient bandwidth to balance ETE and STE, explaining their relatively stable energy consumption as subchannels increase. The FDPC exhibits the best and most stable ETE performance because each UAV is allocated exclusive subchannels, enabling stable data transmission in each time slot. Additionally, by integrating power control, FDPC can adjust transmit power according to factors such as the number of allocated channels, its own transmission tasks, and channel gains.

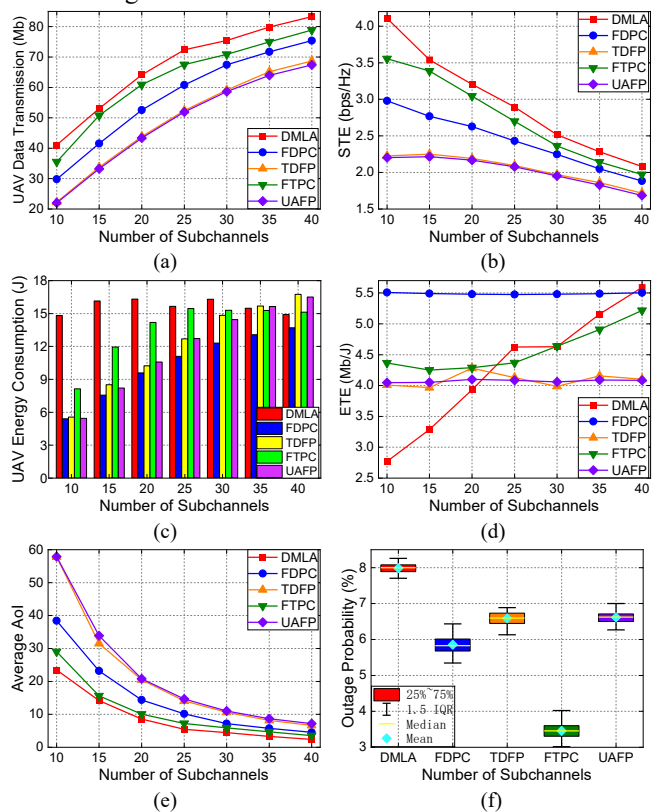


Fig. 5. Performance comparison of different schemes to  $\mathbb{L}2$  under different number of subchannels.

Fig. 5 (e) and Fig. 5 (f) show the average AoI and outage probability, where the outage probability is inferred from the ratio of outage signals to total signals based on the law of large numbers. The figures reveal an inverse correlation between the AoI of each scheme and its previously analyzed transmission capacity. As the number of subchannels increases, AoI reduction trend gradually flattens or even ceases, indicating bandwidth saturation where energy capacity becomes the primary limiting factor. We can learn that excessive bandwidth allocation fails to further improve transmission efficiency and may cause resource waste, necessitating consideration of other bottleneck resources. Moreover, although DMLA achieves the

best transmission performance, it exhibits the highest outage probability. This occurs because NOMA enables multiple UAVs to share a single subchannel, intensifying inter-group interference and reducing the transmission rate per subchannel per UAV. However, the overall UAV throughput increases due to multi-subchannel multiplexing. In contrast, FTPC demonstrates the lowest outage probability, benefiting from finer time division that allows UAVs to dynamically adjust transmit power according to environmental changes, ensuring communication continuity.

### 3) Resource Allocation Comparison of Different Integrated Solutions to $\mathbb{G}^P$

Fig. 6 (a), 6 (b), 6 (c), and 6 (d) demonstrate the minimum number of SATs required for each scheme to achieve S-AoI proportions below 15%, 10%, 5%, and 1% under different numbers of subchannels in a single-LEO scenario. Firstly, as the number of subchannels increases, the transmission capability of each scheme enhances, reducing the AoI of data packets. This necessitates deploying more SATs to decrease the inter-satellite distance, thereby lowering the S-AoI. Secondly, the number of required SATs exhibits an inverse correlation with transmission capability. IS-UAV-DMLA and IS-UAV-FTPC demand more SATs than the other three schemes due to their superior transmission performance, which imposes stricter requirements on AoI.

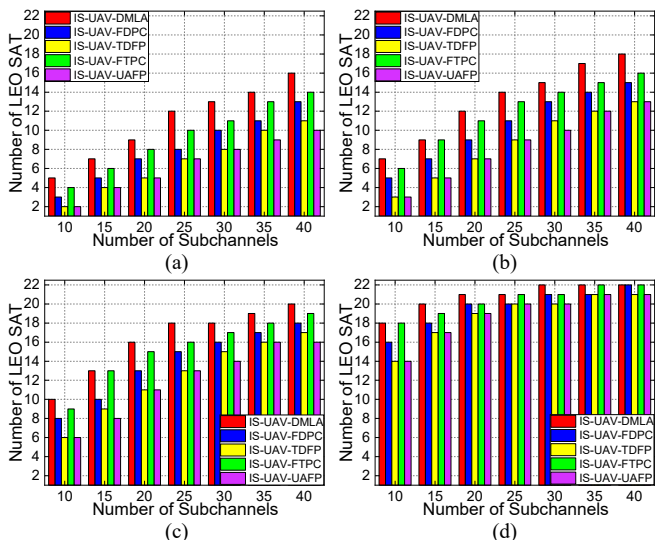


Fig. 6. The required numbers of SATs in a single-LEO under different S-AoI.

Finally, the figures reveal that as the S-AoI proportion decreases, the minimum number of required SATs increases. Notably, the number of SATs needed to reduce the S-AoI proportion from 5% to 1% is greater than that from 15% to 10%, indicating that during SAT service waiting periods, the AoI of UAVs continues to increase. Long waiting times make the deployment of a small number of SATs significantly improve transmission performance. Conversely, as waiting times shorten and UAVs obtain more data transmission opportunities, the incremental effect of additional SATs on performance becomes limited. In practical applications, communication scenarios with low AoI-efficiency requirements exhibit a certain tolerance for satellite coverage density. By contrast, in AoI-sensitive real-time communication scenarios, a denser

satellite network must be deployed to meet stringent performance demands.

### 4) AoI and Single-LEO SAT Density Expression

In light of the aforementioned experimental results analysis, we attempt to derive the expected values of G2A-AoI, A2S-AoI, and S-AoI proportion, respectively.

a) *G2A-AoI Expected Value*: The probability that GT- $n$  is covered by UAV- $m$ , the coverage set when UAV- $m$  covers GT- $n$ , and the scheduling probability when GT- $n$  is covered by UAV- $m$  are denoted as  $q_{n,m}^C$ ,  $\hat{\mathcal{N}}_m^G = \{n | c_{n,m} = 1, \forall n \in \mathcal{V}^G\}$ , and  $q_{n,m}^S$ , respectively.  $q_{n,m}^S$  is calculated as

$$q_{n,m}^S = \begin{cases} 1, & \text{if } |\hat{\mathcal{N}}_m^G| \leq Y^U \\ \frac{|\{i | \ell_i < \ell_n, \forall i \in \hat{\mathcal{N}}_m^G\}|}{|\hat{\mathcal{N}}_m^G|}, & \text{if } |\hat{\mathcal{N}}_m^G| > Y^U \end{cases} \quad (50)$$

Given the possibility of multiple UAVs covering a single GT, directly calculating the GT scheduling probability is challenging. Therefore, we adopt the probability complement rule. First, compute the probability that GT fails to connect to all UAVs, then subtract this value from 1 to obtain the successful scheduling probability. The scheduling interval of GT- $n$  follows a geometric distribution with an expectation of  $\frac{1}{(1 - \prod_{m=1}^M (1 - q_{n,m}^C q_{n,m}^S))}$ . Since AoI increases linearly between two successful transmissions and GT packet generation follows a Poisson distribution, the AoI of GT packets adheres to a discrete uniform distribution [48]. Consequently, the expected AoI value per packet for G2A communication can be expressed as

$$\mathbb{E}[A^G] = \frac{1}{2N} \sum_{n=1}^N \min\left(\frac{\bar{d}_n^G}{\bar{D}_n^G}, 1\right) \left(\frac{1}{(1 - \prod_{m=1}^M (1 - q_{n,m}^C q_{n,m}^S))} + 1\right), \quad (51)$$

where  $\bar{d}_n^G$  is the average size of GT- $n$ 's data packets, and  $\bar{D}_n^G$  is the average data volume transmissible per time slot for GT- $n$  as calculated via (6). It can be inferred from (51) that coverage probability and transmission capability exert significant impacts on the expected value of G2A-AoI, which are primarily positively correlated with UAV path planning and transmission rate. Our IS-UAV architecture has demonstrated superior performance in this regard in the preceding comparison experiments. Additionally, we have optimized GT scheduling, which also affects G2A-AoI, by assigning each GT a priority  $\ell_n(t)$  that comprehensively balances AoI and fairness.

b) *A2S-AoI and Single-LEO SAT Density Expression*: According to single-LEO coverage model, the actual service duration of SAT- $l^k$  for the area of interest is  $T_{m,l^k}^S = \min(T^k, T_{m,l^k})$ , and the waiting time of UAV- $m$  for SAT- $l^k$ 's service is  $T_{m,l^k}^W = \max(T^k - T_{m,l^k}, 0)$ , where  $T^k = \frac{2\pi(d_E + h_k)}{L^S V^S}$  is the SAT interval of LEO- $k$ . Therefore, based on the discrete uniform distribution, the expected AoI value per packet for A2S communication can be expressed as

$$\mathbb{E}[A^G] = \frac{1}{mL^S} \sum_{l^k \in \mathcal{V}^k} \sum_{m=1}^M \left( \frac{T_{m,l^k}^W}{T^k} \left( \frac{T_{m,l^k}^W + 1}{2} + \frac{\bar{d}_m^U}{\bar{D}_m^U} \right) + \frac{T_{m,l^k}^S}{T^k} \frac{\bar{d}_m^U}{\bar{D}_m^U} \right), \quad (52)$$

where  $\bar{d}_m^U$  is the average size of UAV- $m$  data packets, and  $\bar{D}_m^U$  is the average data volume transmissible per time slot for UAV- $m$  as calculated via (24). Furthermore, the expected value of S-AoI proportion for data packets is computed as

$$\mathbb{E}[\partial] = \frac{\sum_{l^k \in \mathcal{V}^k} \sum_{m=1}^M \binom{T_{m,l^k}^W}{m L^S \mathbb{E}[A^G] + \mathbb{E}[A^G]}}{m L^S \mathbb{E}[A^G] + \mathbb{E}[A^G]} \quad (53)$$

Let the S-AoI proportion range  $\partial^S$  be  $[\partial_{min}, \partial_{max}]$ , so that  $\partial_{min} \leq \mathbb{E}[\partial] \leq \partial_{max}$ . This allows the calculation of the minimum and maximum expected values of  $L^S$ , based on which  $L^{max}$  and  $L^{min}$  in Step 5 of Algorithm 2 are set. This enables Algorithm 2 to quickly find the number of single-LEO SATs matching the actual communication scenario within a short time, while avoiding algorithm search failures caused by  $L^{max}$  and  $L^{min}$  exceeding the feasible region.

## VII. CONCLUSIONS

To address communication disruptions caused by GBS failures in post-disaster areas, we proposed the PDPCIN framework, which integrates UAV-enabled WDC/WET and utilizes LEO satellites to forward data to the nearest operational GBS. To guarantee fundamental connectivity while collaborative optimizing AoI, energy, and spectrum efficiency, we designed three key components of PDPCIN: the AFTU mechanism for dynamic GT type updates, the IS-UAV architecture for concurrent WDC and WET, and the DMLOA strategy for coordinated scheduling across multiple UAVs and satellites. Given the MINLP nature of the global problem  $\mathbb{G}\mathbb{P}$ , we developed the HHGNN framework, which models heterogeneous devices and their communication relations as a hierarchical heterogeneous graph using customized G3Ms. HHGNN decompose  $\mathbb{G}\mathbb{P}$  into two layers:  $\mathbb{L}1$ , which optimizes UAV 3D trajectories and WET decisions; and  $\mathbb{L}2$ , which focuses on UAV-LEO scheduling, power control, and subchannel allocation, based on  $\mathbb{L}1$  outcomes. Both subproblems are modeled as MDPs. To further investigate how the number of satellites in a single LEO affects AoI and spectrum efficiency under S-AoI constraints, we introduced the S-LSDO algorithm, which employs binary search-based iterative optimization to identify the optimal SAT count. Extensive simulations show that our approach outperforms existing benchmarks in collaborative optimizing AoI, energy, and spectrum performance. Based on this, we further derived the expressions for the expected values of AoI and S-AoI proportion to guide resource allocation in PDPCIN. In our future work, we will consider more practical scenarios, such as signal outages among GTs due to interference, and explore the application of next generation multiple access (NGMA) techniques to mitigate inter-UAV interference and further improve bandwidth utilization. Additionally, we will investigate integrating large language model-enhanced reinforcement learning to improve the expressiveness of GNNs and the generalization of algorithms.

## ACKNOWLEDGEMENT

This work was supported in part by the National Natural Science Foundation of China (62272484, 61873352).

## REFERENCES

- [1] W. A. Nelson, S. R. Yeduri, A. Jha, A. Kumar, and L. R. Cenkeramaddi, "RL-Based Energy-Efficient Data Transmission Over Hybrid BLE/LTE/Wi-Fi/LoRa UAV-Assisted Wireless Network," *IEEE/ACM Trans. Netw.*, vol. 32, no. 3, pp. 1951-1966, Jun. 2024, doi: 10.1109/TNET.2023.3332296.
- [2] C. Zhou, J. Liu, K. Qu, M. Sheng, J. Li, and W. Zhuang, "Delay-Aware UAV Computation Offloading and Communication Assistance for Post-Disaster Rescue," *IEEE Trans. Wireless Commun.*, vol. 23, no. 12, pp. 19110-19125, Dec. 2024, doi: 10.1109/TWC.2024.3479709.
- [3] ITU-R, "Framework and overall objectives of the future development of IMT for 2030 and beyond," *Int. Telecommun. Union, Rec. ITU-R M.2160-0*, Nov. 2023. [Online]. Available: <https://www.itu.int/rec/R-REC-M.2160/en>.
- [4] Y. Li et al., "Data Collection Maximization in IoT-Sensor Networks via an Energy-Constrained UAV," *IEEE Trans. Mobile Comput.*, vol. 22, no. 1, pp. 159-174, Jan. 2023, doi: 10.1109/TMC.2021.3084972.
- [5] S. Chai and V. K. N. Lau, "Multi-UAV Trajectory and Power Optimization for Cached UAV Wireless Networks With Energy and Content Recharging-Demand Driven Deep Learning Approach," *IEEE J. Sel. Areas Commun.*, vol. 39, no. 10, pp. 3208-3224, Oct. 2021, doi: 10.1109/JSAC.2021.3088694.
- [6] B. Zhu, E. Bedeer, H. H. Nguyen, R. Barton, and Z. Gao, "UAV Trajectory Planning for AoI-Minimal Data Collection in UAV-Aided IoT Networks by Transformer," *IEEE Trans. Wireless Commun.*, vol. 22, no. 2, pp. 1343-1358, Feb. 2023, doi: 10.1109/TWC.2022.3204438.
- [7] Y. Gao, X. Yuan, D. Yang, Y. Hu, Y. Cao, and A. Schmeink, "UAV-Assisted MEC System With Mobile Ground Terminals: DRL-Based Joint Terminal Scheduling and UAV 3D Trajectory Design," *IEEE Trans. Veh. Technol.*, vol. 73, no. 7, pp. 10164-10180, Jul. 2024, doi: 10.1109/TVT.2024.3367624.
- [8] R. Wang, M. A. Kishk, and M. -S. Alouini, "Ultra Reliable Low Latency Routing in LEO Satellite Constellations: A Stochastic Geometry Approach," *IEEE J. Sel. Areas Commun.*, vol. 42, no. 5, pp. 1231-1245, May 2024, doi: 10.1109/JSAC.2024.3365884.
- [9] Z. Lai, H. Li, Q. Zhang, Q. Wu, and J. Wu, "StarFront: Cooperatively Constructing Pervasive and Low-Latency CDNs Upon Emerging LEO Satellites and Clouds," *IEEE/ACM Trans. Netw.*, vol. 31, no. 6, pp. 2559-2574, Dec. 2023, doi: 10.1109/TNET.2023.3260166.
- [10] N. Guo, L. Liu, and X. Zhong, "Task-Aware Distributed Inter-Layer Topology Optimization Method in Resource-Limited LEO-LEO Satellite Networks," *IEEE Trans. Wireless Commun.*, vol. 23, no. 4, pp. 3572-3585, Apr. 2024, doi: 10.1109/TWC.2023.3309379.
- [11] C. Liu et al., "FERN: Leveraging Graph Attention Networks for Failure Evaluation and Robust Network Design," *IEEE/ACM Trans. Netw.*, vol. 32, no. 2, pp. 1003-1018, Apr. 2024, doi: 10.1109/TNET.2023.3311678.
- [12] O. S. Oubbati, M. Atiquzzaman, H. Lim, A. Rachedi, and A. Lakas, "Synchronizing UAV Teams for Timely Data Collection and Energy Transfer by DRL," *IEEE Trans. Veh. Technol.*, vol. 71, no. 6, pp. 6682-6697, Jun. 2022, doi: 10.1109/TVT.2022.3165227.
- [13] H. Pan, Y. Liu, G. Sun, J. Fan, S. Liang, and C. Yuen, "Joint Power and 3D Trajectory Optimization for UAV-Enabled Wireless Powered Communication Networks With Obstacles," *IEEE Trans. Commun.*, vol. 71, no. 4, pp. 2364-2380, Apr. 2023, doi: 10.1109/TCOMM.2023.3240697.
- [14] M. Li, H. Li, P. Ma, and H. Wang, "Energy Maximization for Ground Nodes in UAV-Enabled Wireless Power Transfer Systems," *IEEE Internet Things J.*, vol. 10, no. 19, pp. 17096-17109, Oct. 1, 2023, doi: 10.1109/IIOT.2023.3274549.
- [15] Y. Zhou, Z. Jin, H. Shi, L. Shi, and N. Lu, "Flying IRS: QoE-Driven Trajectory Optimization and Resource Allocation Based on Adaptive Deployment for WPCNs in 6G IoT," *IEEE Internet Things J.*, vol. 11, no. 5, pp. 9031-9046, Mar. 1, 2024, doi: 10.1109/IIOT.2023.3322266.
- [16] C. Kim, H. -H. Choi, and K. Lee, "Joint Optimization of Trajectory and Resource Allocation for Multi-UAV-Enabled Wireless-Powered Communication Networks," *IEEE Trans. Commun.*, vol. 72, no. 9, pp. 5752-5764, Sept. 2024, doi: 10.1109/TCOMM.2024.3383113.
- [17] Q. Tang, Y. Yang, H. Yang, D. Cao, and K. Yang, "Energy Consumption Minimization for Hybrid Federated Learning and Offloadable Tasks in UAV-Enabled WPCN," *IEEE Trans. Netw. Sci. Eng.*, vol. 11, no. 5, pp. 4639-4650, Sept.-Oct. 2024, doi: 10.1109/TNSE.2024.3422658.
- [18] Z. Y. Zhao, Y. L. Che, S. Luo, G. Luo, K. Wu, and V. C. M. Leung, "On Designing Multi-UAV Aided Wireless Powered Dynamic Communication via Hierarchical DRL," *IEEE Trans. Mobile Comput.*, vol. 23, no. 12, pp. 13991-14004, Dec. 2024, doi: 10.1109/TMC.2024.3439556.
- [19] X. Liu, H. Liu, K. Zheng, J. Liu, T. Taleb, and N. Shiratori, "AoI-Minimal Clustering, Transmission and Trajectory Co-Design for UAV-Assisted WPCNs," *IEEE Trans. Veh. Technol.*, vol. 74, no. 1, pp. 1035-1051, Jan. 2025, doi: 10.1109/TVT.2024.3461333.

- [20] Q. Xu, Z. Su, D. Fang, and Y. Wu, "Hierarchical Bandwidth Allocation for Social Community-Oriented Multicast in Space-Air-Ground Integrated Networks," *IEEE Trans. Wireless Commun.*, vol. 22, no. 3, pp. 1915-1930, Mar. 2023, doi: 10.1109/TWC.2022.3207923.
- [21] S. Zhang, T. Cai, D. Wu, D. Schupke, N. Ansari, and C. Cavdar, "IoRT Data Collection With LEO Satellite-Assisted and Cache-Enabled UAV: A DRL Approach," *IEEE Trans. Veh. Technol.*, vol. 73, no. 4, pp. 5872-5884, Apr. 2024, doi: 10.1109/TVT.2023.3336262.
- [22] C. Huang, G. Chen, P. Xiao, Y. Xiao, Z. Han, and J. A. Chambers, "Joint Offloading and Resource Allocation for Hybrid Cloud and Edge Computing in SAGINs: A Decision Assisted Hybrid Action Space DRL Approach," *IEEE J. Sel. Areas Commun.*, vol. 42, no. 5, pp. 1029-1043, May 2024, doi: 10.1109/JSAC.2024.3365899.
- [23] Y. Wang et al., "E2E Network Slicing Optimization for Control- and User-Plane Separation-Based SAGINs With DRL," *IEEE Trans. Veh. Technol.*, vol. 73, no. 11, pp. 16680-16696, Nov. 2024, doi: 10.1109/TVT.2024.3415964.
- [24] Y. Gao, Z. Ye, and H. Yu, "Cost-Efficient Computation Offloading in SAGIN: A DRL and Perception-Aided Approach," *IEEE J. Sel. Areas Commun.*, vol. 42, no. 12, pp. 3462-3476, Dec. 2024, doi: 10.1109/JSAC.2024.3459073.
- [25] J. Li et al., "Active RIS-Aided NOMA-Enabled Space-Air-Ground Integrated Networks With Cognitive Radio," *IEEE J. Sel. Areas Commun.*, vol. 43, no. 1, pp. 314-333, Jan. 2025, doi: 10.1109/JSAC.2024.3460067.
- [26] J. Tan, F. Tang, M. Zhao, and N. Kato, "Outage Probability, Performance, and Fairness Analysis of Space-Air-Ground Integrated Network (SAGIN): UAV Altitude and Position Angle," *IEEE Trans. Wireless Commun.*, vol. 24, no. 2, pp. 940-954, Feb. 2025, doi: 10.1109/TWC.2024.3503060.
- [27] H. Liu and J. Gui, "Spectrum-Energy Efficient Sink-AAV-LEO Backbone Networks to Ensure Ubiquitous Data Collection Timeliness," *IEEE Internet Things J.*, vol. 12, no. 9, pp. 12761-12776, May 1, 2025, doi: 10.1109/JIOT.2024.3522344.
- [28] Q. Wei, Y. Chen, Z. Jia, W. Bai, T. Pei, and Q. Wu, "Energy-Efficient Caching and User Selection for Resource-Limited SAGINs in Emergency Communications," *IEEE Trans. Commun.*, vol. 73, no. 6, pp. 4121-4136, Jun. 2025, doi: 10.1109/TCOMM.2024.3511958.
- [29] X. Zhang, H. Zhao, J. Wei, C. Yan, J. Xiong, and X. Liu, "Cooperative Trajectory Design of Multiple UAV Base Stations With Heterogeneous Graph Neural Networks," *IEEE Trans. Wireless Commun.*, vol. 22, no. 3, pp. 1495-1509, Mar. 2023, doi: 10.1109/TWC.2022.3204794.
- [30] Z. Guo et al., "UWTracking: Passive Human Tracking Under LOS/NLOS Scenarios Using IR-UWB Radar," *IEEE Trans. Mobile Comput.*, vol. 23, no. 12, pp. 11853-11870, Dec. 2024, doi: 10.1109/TMC.2024.3404460.
- [31] C. E. Garcia, M. R. Camana, J. Querol, and S. Chatzinotas, "Rate-Splitting Multiple Access for Secure Communications Over CR MISO SWIPT Systems With Non-Linear EH Users," *IEEE Trans. Green Commun. Netw.*, vol. 8, no. 4, pp. 1332-1347, Dec. 2024, doi: 10.1109/TGCN.2024.3404891.
- [32] A. Naha and S. Dey, "Bayesian Quickest Change-Point Detection With an Energy Harvesting Sensor and Asymptotic Analysis," *IEEE Trans. Signal Process.*, vol. 72, pp. 565-579, 2024, doi: 10.1109/TSP.2024.3350340.
- [33] J. Shi, P. Cong, L. Zhao, X. Wang, S. Wan, and M. Guizani, "A Two-Stage Strategy for UAV-Enabled Wireless Power Transfer in Unknown Environments," *IEEE Trans. Mobile Comput.*, vol. 23, no. 2, pp. 1785-1802, Feb. 2024, doi: 10.1109/TMC.2023.3240763.
- [34] S. Zhang, Y. Mao, B. Clerckx, and T. Q. S. Quek, "Interference Management in Space-Air-Ground Integrated Networks With Fully Distributed Rate-Splitting Multiple Access," *IEEE Trans. Wireless Commun.*, vol. 24, no. 1, pp. 149-164, Jan. 2025, doi: 10.1109/TWC.2024.3489219.
- [35] M. D. Nguyen, L. B. Le, and A. Girard, "Integrated Computation Offloading, UAV Trajectory Control, Edge-Cloud and Radio Resource Allocation in SAGIN," *IEEE Trans. Cloud Comput.*, vol. 12, no. 1, pp. 100-115, Jan.-Mar. 2024, doi: 10.1109/TCC.2023.3339394.
- [36] Z. Zhang, Y. Wu, Z. Ma, X. Lei, L. Lei, and Z. Wei, "Coordinated Multi-Satellite Transmission for OTFS-Based 6G LEO Satellite Communication Systems," *IEEE J. Sel. Areas Commun.*, vol. 43, no. 1, pp. 156-170, Jan. 2025, doi: 10.1109/JSAC.2024.3460108.
- [37] L. You et al., "Integrated Communications and Localization for Massive MIMO LEO Satellite Systems," *IEEE Trans. Wireless Commun.*, vol. 23, no. 9, pp. 11061-11075, Sept. 2024, doi: 10.1109/TWC.2024.3378305.
- [38] E. Kim, I. P. Roberts, and J. G. Andrews, "Downlink Analysis and Evaluation of Multi-Beam LEO Satellite Communication in Shadowed Rician Channels," *IEEE Trans. Veh. Technol.*, vol. 73, no. 2, pp. 2061-2075, Feb. 2024, doi: 10.1109/TVT.2023.3312977.
- [39] K. Ying et al., "Quasi-Synchronous Random Access for Massive MIMO-Based LEO Satellite Constellations," *IEEE J. Sel. Areas Commun.*, vol. 41, no. 6, pp. 1702-1722, Jun. 2023, doi: 10.1109/JSAC.2023.3273699.
- [40] Y. Liu and H. Cheng, "Outage Performance Analysis and Optimization of Two-User Downlink NOMA Systems With Imperfect SIC and Improper Signaling," *IEEE Trans. Wireless Commun.*, vol. 23, no. 9, pp. 11649-11661, Sept. 2024, doi: 10.1109/TWC.2024.3384147.
- [41] Y. Liu, K. Xiong, Y. Zhu, H. -C. Yang, P. Fan, and K. B. Letaief, "Outage Analysis of IRS-Assisted UAV NOMA Downlink Wireless Networks," *IEEE Internet Things J.*, vol. 11, no. 6, pp. 9298-9311, Mar. 15, 2024, doi: 10.1109/JIOT.2023.3323311.
- [42] J. Gui and F. Cai, "Coverage Probability and Throughput Optimization in Integrated mmWave and Sub-6 GHz Multi-UAV-Assisted Disaster Relief Networks," *IEEE Trans. Mobile Comput.*, vol. 23, no. 12, pp. 10918-10937, Dec. 2024, doi: 10.1109/TMC.2024.3386550.
- [43] S. Brody, U. Alon, and E. Yahav, "How Attentive are Graph Attention Networks?," in *ICLR*, 2022.
- [44] C. Meng, M. Tang, M. Setayesh, and V. W. S. Wong, "Tackling Resource Allocation for Decentralized Federated Learning: a GNN-based Approach," *IEEE Trans. Mobile Comput.*, doi: 10.1109/TMC.2025.3562834.
- [45] A. Wijesinghe and Q. Wang, "A new perspective on" how graph neural networks go beyond weisfeiler-lehman?," in *International Conference on Learning Representations*, 2022.
- [46] J. -H. Lee, H. Seo, J. Park, M. Bennis, and Y. -C. Ko, "Learning Emergent Random Access Protocol for LEO Satellite Networks," *IEEE Trans. Wireless Commun.*, vol. 22, no. 1, pp. 257-269, Jan. 2023, doi: 10.1109/TWC.2022.3192365.
- [47] Y. Liu, J. Yan, and X. Zhao, "Deep-Reinforcement-Learning-Based Optimal Transmission Policies for Opportunistic UAV-Aided Wireless Sensor Network," *IEEE Internet Things J.*, vol. 9, no. 15, pp. 13823-13836, Aug. 1, 2022, doi: 10.1109/JIOT.2022.3142269.
- [48] C. H. Weiß, "The Mollified (Discrete) Uniform Distribution and Its Applications," *Wiley Interdiscip. Rev. Comput. Stat.*, vol. 17, no. 1, Art. no. e70016, Mar. 2025, doi: 10.1002/wics.70016.